Physics – Uspekhi **68** (9) 883 – 904 (2025)

REVIEWS OF TOPICAL PROBLEMS

PACS numbers: 43.25.Cb, 43.40.Jc, 52.25.Kn, 52.35.Tc, 64.30.Jk

Properties of nonideal plasma of noble gases and nitrogen shock compressed to 1 TPa

M.A. Mochalov, R.I. Ilkaev

DOI: https://doi.org/10.3367/UFNe.2025.02.039874

Contents

Abstract. Results of experimental studies of compressibility, sound velocity, temperature, electrical conductivity, absorption, and reflection of light under shock compression of noble gases (argon, krypton, xenon) and liquid nitrogen are presented. Experiments were carried out at VNIIEF using condensed explosives in the pressure range up to $P \approx 1$ TPa. Experimental devices for producing and diagnosing states with high energy density are described. The data obtained were used to test and refine models of equations of state, when strong interparticle interaction affects the properties of substances, in the hard-to-calculate region of high-pressure nonideal plasma. Newly obtained and existing information on the properties of nonideal plasma of the materials studied is analyzed.

Keywords: nonideal plasma, noble gases, nitrogen, Hugoniot adiabat, speed of sound, temperature, electrical conductivity, equation of state

1. Introduction

The modern physics of high energy densities explores states with an energy concentration in matter above $10^4 - 10^5$ J cm^{-3} commensurate with the binding energy of atoms in condensed media and a pressure of millions of atmospheres. High energy density in such objects causes thermal ionization and/or pressure ionization. As a result, a nonideal plasma arises, where the energy of Coulomb interaction between particles is comparable to or exceeds the kinetic energy of particle motion, and the effects of electron degeneracy are significant for calculating the equations of state (EOSs) and the degree of ionization of such plasma. In such states, the theory predicts some qualitatively new physical phenomena, such as metallization, plasma phase transitions, and dielectricization, which must be taken into account when constructing the EOS of highly compressed plasma. Basic studies of the properties of extreme-state plasma are directly related to solving technical problems of its application in various power plants of the future, where such plasma can be employed as a working fluid. Without new information on the physical properties of nonideal plasma in the megabar pressure range, it is not possible to interpret terrestrial and space measurement data, or to construct, based on these data, models of the evolution, structure, and energy of objects. This information is needed in a wide range of state parameters, of which only a small part is currently accessible for laboratory measurements. The studies of the properties of nonideal plasma carried out under the guidance of Academician V.E. Fortov by his colleagues [1–9], which led to the creation of a new field of physics — the dynamic physics of dense plasma [10] — have been widely recognized all over the world.

Basic information on the behavior of substances at high temperatures and pressures was obtained by measuring compressibility in shock-wave experiments. In some cases, shock adiabats are the only source of data on the forces of interparticle interaction, knowledge of which is necessary for the theoretical substantiation of the equations of state of the substances under study. Cryogenic liquids of the noble gases (argon, krypton, and xenon), which feature the simplest structure, are ideal for examining their properties by the shock compression method. High initial densities (for example, in xenon $\rho_0 = 2.96$ g cm^{-3} at $T = 165$ K) make it possible to achieve pressures of ~ 100–1000 GPa and densities of $\sim 10 - 20$ g cm^{-3} in physical experiments. Due to the transparency of liquefied gases, there are no fundamental limitations on detecting the radiation of the shock wave front through a layer of a substance that has not yet

M.A. Mochalov (*), **R.I. Ilkaev**
Russian Federal Nuclear Center–All-Russian Research Institute of Experimental Physics,
prosp. Mira 37, 607190 Sarov, Nizhny Novgorod region, Russian Federation
E-mail: (*) postmaster@ifv.vniief.ru

Received 30 November 2024, revised 18 January 2025
Uspekhi Fizicheskikh Nauk **195** (9) 931 – 961 (2025)
Translated by M.Zh. Shmatikov

been compressed. It was in experiments with noble gases that new phenomena arising during shock compression were first discovered and studied. Their common feature is the electronic excitation of an atom when the electron shells overlap due to strong compression, which leads to a narrowing and then to complete closure of the energy gap. Since these effects are interrelated, it is necessary to supplement shock compression measurements with experiments to study electrical conductivity and temperature. The role of electronic excitation is determined indirectly by the deviation of the experimental adiabats from the theoretical ones, while the parameters of electron structure models are theoretically determined from a comparison with experiment.

By now, dynamic methods have been developed that enable advancement in the study of the physical properties of substances in a wide region of the phase diagram, extending from densities corresponding to solid and dense liquid-metal states to nonideal plasma states obtained during isentropic expansion of shock-compressed materials.

As regards the topic of this review, highly nonideal plasma was explored during shock compression of gaseous argon, nitrogen, and xenon in [11–14]. The method of shock compression using condensed explosives and a two-cascade light-gas accelerator was also used to study the compressibility of liquid argon on the main and reflected Hugoniot adiabats [15–22], solid argon [23], liquid xenon [24], nitrogen [25–30], oxygen [17, 31], and air [32]. Currently, shock compression of argon, xenon, krypton, and nitrogen in the pressure range up to 1000 GPa are being studied using the Z machine and the Omega laser setup [33–37].

Most studies that investigated compressibility did not include measurements of the temperature of the shock-compressed media, which is an additional and often more sensitive parameter for testing various theories than the shock compression pressure alone. Experimental measurement of temperatures in shock-wave experiments is important for constructing a thermodynamically complete equation of state, since it makes it possible to independently test its parameters, in particular, the behavior of heat capacity at high degrees of compression. In addition, knowledge of temperature is essential for studying such phenomena as dielectric–metal transitions, melting, dissociation, and ionization.

Presented below are the experimental data obtained at VNIIEF in studying thermophysical properties of noble gases (argon, krypton, and xenon) and liquid nitrogen during their shock compression using condensed explosives. The attention to the study of the noble gas properties is due to the need to exclude the influence of dissociation on the processes occurring in substances under extreme conditions. On the other hand, experiments with liquid nitrogen are necessary precisely to study the role of dissociation during shock compression, which can be accompanied by the excitation of intramolecular vibrations and, concurrently, electronic degrees of freedom, the rupture of chemical bonds in molecules, or the formation of stable compact structures or new phases with a certain degree of electron collectivization. A specific feature of molecular nitrogen is that it can form clusters with double and single bonds, which is manifested in the ability to form, in addition to a molecular crystal and molecular fluid, various types of polymeric states. The existence of the transition between the molecular and polymer phases of nitrogen as a first-order phase transition was predicted in [38] with the critical point parameters $T_c = 11500$ K and $P_c = 6$ GPa and confirmed in *ab initio* calculations using the quantum molecular dynamics method [39], but with the critical point parameters $T_c = 4-5$ kK and $P_c = 50-70$ GPa, which differ significantly from the estimates reported in [38]. The problem of experimental localization of the boundaries of the molecular, polymer, and plasma states of nitrogen drives increased interest in studying its properties in the region of high pressures and temperatures.

For the studies outlined above, cryogenic experimental devices of flat and hemispherical geometry were developed at VNIIEF and diagnostic methods were applied, including recording of kinematic and thermodynamic parameters, reflection and absorption coefficients of light, and conductivity of the substances under study. In the VNIIEF experiments, shock-wave compressibility and temperature were measured concurrently in shock-compressed liquid argon [40, 41], xenon [42–44], krypton [45, 46], and nitrogen [47–49] up to $T \sim 60{,}000$ K in the pressure range up to ~ 500 GPa. A slowdown in the rate of temperature increase in liquefied noble gases with an increase in the shock wave amplitude in the pressure range above 30–40 GPa was observed, which is associated with the kinetics of excitation of electrons from the valence band to the conduction band.

During measurements of the electrical conductivity of noble gases, an effect of a sharp increase in the number of current carriers, electrons, was discovered, along with a sharp increase in conductivity accompanying this phenomenon at the pressures achieved in the experiments [50, 51].

The generally accepted approach to constructing equations of state in the areas of the phase diagram where theoretical models do not provide acceptable accuracy consists of developing semi-empirical approaches in which the type of functional dependences is established on the basis of clear physical concepts, and the set of experimental data is used to determine the numerical values of the free parameters in these dependences. The scope of applicability of empirical and interpolation EOSs is determined by both the physical content of the models and the volume of experimental information used to determine the fitting (free) parameters of the experimental information used in the models. Such an approach allows constructing EOSs in a compact form convenient for numerical modeling with maximum use of experimental data.

To describe the experimental data, equations of state for argon [40, 41] and xenon [42–44] in the solid and liquid phases were constructed at VNIIEF using the technique tested in [52–54] as applied to the equations of state of metals. Subsequently, for comparison with experimental data, a chemical model of plasma was used [55] that takes into account the effects of Coulomb interaction of charged particles, electron degeneracy, changes in the contribution of bound states during compression of matter, and short-range repulsion of atoms and ions at close distances. Today, first-principles modeling methods — density functional theory (DFT) and quantum Monte Carlo (QMC) — are widely used. Both methods were used in [33–37] to describe data on the compressibility of noble gases and nitrogen and to describe krypton in the VNIIEF experiments [46]. Calculations using models from the SESAME library [56] were also used for comparison with experimental data.

The experience of computational and theoretical studies shows that, to enhance the quality of model EOSs along with a significant reduction in the costs of conducting experiments, it is necessary to develop systems for generating and

diagnosing the states of substances with high energy density, allowing one to simultaneously obtain various reliable experimental information on the thermodynamic, optical, and electrophysical properties of nonideal plasma. The experiments described below meet these requirements. We focused on the presentation of experimental data obtained in various laboratories around the world. To describe the experimental data, the calculated dependences from the original publications were used without discussing theoretical approximations.

2. Shock-wave compression

Experiments on shock-wave compression measure the kinematic parameters of the shock wave: its velocity D and the mass velocity of the substance behind the front U. Based on these data and applying the laws of conservation of mass, momentum, and energy, the pressure P, density ρ, and internal energy of the shock-compressed substance E are found:

$$\begin{cases} \rho(D-U) = \rho_0 D\,, \\ P+\rho(D-U)^2 = P_0+\rho_0 D^2\,, \\ E+\dfrac{P}{\rho}+\dfrac{(D-U)^2}{2} = E_0+\dfrac{P_0}{\rho_0}+\dfrac{D^2}{2}\,. \end{cases} \tag{2.1}$$

In Eqns (2.1), P_0, ρ_0, E_0 are, respectively, the pressure, density, and specific internal energy in the initial state.

In VNIIEF studies with liquefied gases, cryostats of flat and hemispherical geometry combined with shock wave generators (SWGs) were used for this purpose. One of the first designs of a cryostat with a flat SWG for experiments in the pressure range up to 100 GPa is displayed in Fig. 1a [40]. The liquefied gas under study (*1*) is located in the internal cavity of the cryostat (*2*), limited from below by a flat metal screen (*3*). The screen, the striker, and the explosive (EX) are elements of the plane-wave SWG developed at VNIIEF, with well-known characteristics (see, for example, [57]). The designs exclude thermal contact of the cooled elements with the surface of the explosive included in the SWG, and provide conditions for eliminating boiling in the liquid under study. The striker is accelerated to a known speed W under the action of expanding explosion products (EPs). Upon collision with the screen, it generates a shock wave in the screen, which then goes out into the liquefied gas, compressing and heating it. Located on the known base (Δ) in the liquid are sensors for measuring the velocity of the shock wave (SW). Through the hole in the center of the diaphragm and the mirror (M), a pyrometer records the radiation, by which the spectral temperature at its front is measured (see below). In early experiments, the SW front radiation was recorded in time on photographic film using a high-speed photo recorder in the red region of the spectrum ($\lambda_{cp} = 670$ nm) (Fig. 1b, variant I), and, in an improved variant, simultaneously in the red and blue ($\lambda_{cp} = 430$ nm) regions of the spectrum (Fig. 1b, variant II). To do so, a combined blue-red light filter was made, through which the radiation of the SW front, limited by a diaphragm, was simultaneously recorded in two spectral intervals. Typical photochronograms of the SW front radiation for two recording methods are shown in Fig. 1b, and a densitogram of the density of blackening of the photographic film for one of these images is displayed in Fig. 1c.

For experiments above 100 GPa, cryogenic devices (Fig. 2) were developed combined with hemispherical SWGs [58]. The

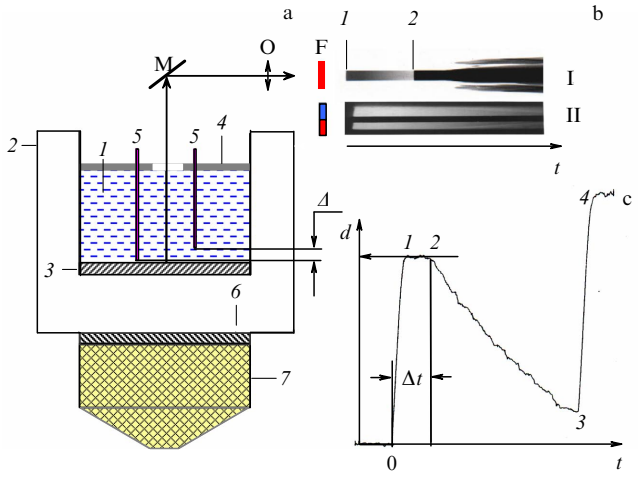

Figure 1. (a) Experimental device with flat SWG for studying kinematic and optical characteristics in shock-compressed cryogenic liquids: *1* — liquefied gas, *2* — cryostat, *3* — screen, *4* — diaphragm, *5* — electric contact sensors, *6* — striker, *7* — SWG, M — mirror, O — objective; (b) photochronogram: *1* — beginning of SW front glow in liquid, *2* — SW exit to liquid-air boundary, F — light filter: (c) densitogram of film blackening (*d* — blackening density). Δt — time from onset of SW front glow to decay of radiation intensity due to decrease in shock compression pressure associated with 'catch-up' of SW front by unloading wave. Section *1–2* — period of constant brightness, section *2–3* — period of decay of shock wave amplitude, section *3–4* — SW exit into air.

design uses optical (k) and electrical contact sensors to measure the SW velocity in the liquid (a–b) and to measure the SW velocity in the screen (c–d). Radiation from the SW front was recorded through a sapphire window (*4*) and a light guide located along the axis of the cryogenic cell in five spectral intervals using a pyrometer [59] in combination with high-speed oscilloscopes. A typical oscillogram of SW front radiation is shown in Fig. 2b. The spectral temperatures of the SW front were measured from the radiation amplitude, while the SW travel time in the liquefied gas $\Delta t_{liq} = t_3 - t_1$ and in the optical window $\Delta t_{port} = t_5 - t_3$ were measured from the characteristic structures on the oscillogram. The increase in radiation in the section $t_1 - t_2$ was used to find the absorption coefficient of light behind the SW front (see below). The presence of a sapphire window leads to the formation of a reflected shock wave, which propagates into the region of the compressed test liquid. In experiments with liquid argon and xenon, the dynamic parameters — pressure P_2 and density ρ_2 in the shock wave reflected from the sapphire window — were determined using the formulas

$$P_2 = P_1 + \rho_1 D_{12} \Delta U_{12}\,, \tag{2.2}$$

$$\rho_2 = \frac{\rho_1 D_{12}}{D_{12} - \Delta U_{12}}\,. \tag{2.3}$$

Here, P_1, U_1, ρ_1 are the pressure, mass velocity, and density of the test liquid on the direct shock wave, P_2 and ρ_2 are the pressure and density in the reflected shock wave, D_{12} is the propagation velocity of the reflected shock wave relative to the substance in front of its front, and $\Delta U_{12} = U_1 - U_2$ is the jump in mass velocity at the front of the reflected shock wave. The pressure in the reflected wave P_2, equal to the pressure in sapphire P_{sap}, is determined from the measured value of the shock wave velocity in sapphire, the adiabat of which is taken from [30].

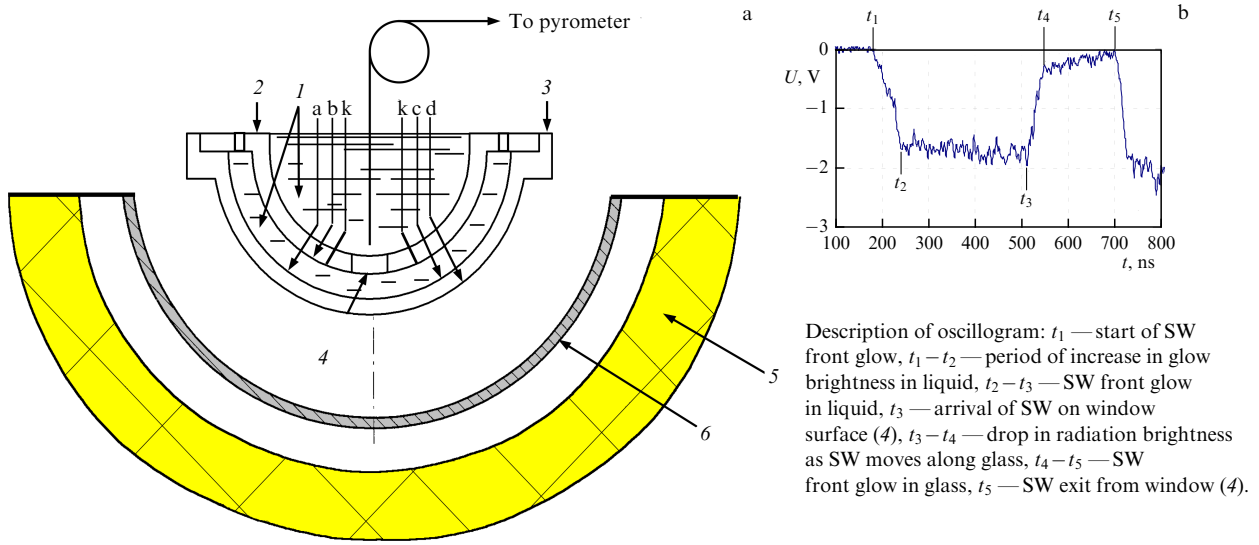

Figure 2. (a) Cryogenic device with hemispherical SWG: *1* — test liquid, *2* — measuring unit, *3* — screen, *4* — optical window (sapphire), *5* — EX, *6* — striker; (b) oscillogram of SW front radiation.

In accordance with the reflection method for determining the pressure and mass velocity in the reflected wave based on the measured values of shock wave velocities in liquefied gas and sapphire, the problem of the decay of an arbitrary discontinuity at the liquefied gas–sapphire interface was solved. The transition from the measured average values of shock wave velocities to instantaneous values at the discontinuity decay boundaries was made by modeling experiments using VNIIEF's one-dimensional gas-dynamic program [60].

In experiments with argon, krypton, and xenon, the high-purity gas under study was condensed immediately before the experiment in a liquefier with liquid nitrogen. The initial temperatures of the liquefied gases, measured in control experiments using a platinum resistor, were $T_0 = 77.3$ K for nitrogen, 86.4 K for argon, 120 K for krypton, and 165 K for xenon (average of 10 measurements). For the measured temperatures, the initial densities of the gases under study were estimated using their equations of state from [61, 62]: $\rho_0 = 0.807$ g cm^{-3} at $T_0 = 77$ K for nitrogen; $\rho_0 = 1.4$ g cm^{-3} at $T_0 = 86.4$ K for argon; $\rho_0 = 2.418$ g cm^{-3} at $T_0 = 120$ K for krypton; and $\rho_0 = 2.96$ g cm^{-3} at $T_0 = 165$ K for xenon.

The experimental devices used aluminum (grade AD-1) or iron (grade St3 steel) screens. When processing the data for aluminum, the equation of state [63] was used, which describes well the experimental results in almost the entire range investigated using shock waves, including data on the adiabats of repeated compression and adiabatic expansion [64–66]. When using iron screens in some experiments, the data were processed using the EOS [67], refined for the region of high pressures and densities. The equations of state of the materials used take into account the change in their density with temperature.

Liquid argon. The compressibility of liquid argon when using condensed EX and in experiments on a light-gas gun was studied up to 91 GPa in [17, 18]. Almost simultaneously, the compressibility of argon up to 65 GPa in the wake of the plane shock wave front was measured at VNIIEF [40], and later, using hemispherical SWGs, up to 250 GPa on the main Hugoniot adiabat and up to 530 GPa on the reflected one [41]. The results of these experiments remained unparalleled for almost 20 years. Recently, in shock-wave experiments using the Z machine at SNL, the compressibility of liquid argon on the main adiabat up to 600 GPa and during repeated compression up to 950 GPa [33] was investigated. In the same study [33], data from three experiments up to 1 TPa, obtained at the Omega laser facility, have been presented. The entire set of $D-U$ data obtained in [17, 18, 33], together with the VNIIEF data [40, 41], is displayed in Fig. 3 and indicates good agreement with results obtained in various laboratories.

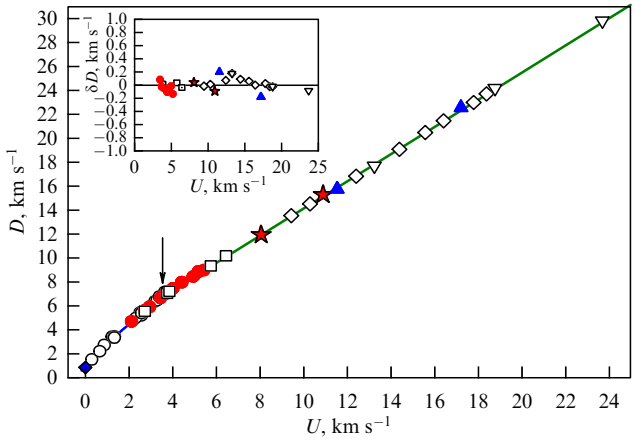

Figure 3. Hugoniot adiabat of liquid argon. Experiment: white dots — [16], white squares — [17, 18], red dots — [40], red stars — [41]; blue diamond is speed of sound in liquid argon at saturation line [62]. Experiment [33]: white diamonds — quartz screen, blue triangles — Al screen; white triangles — quartz screen (Omega setup). Solid black line is linear approximation of data: $D = 2.8092 + 1.1339U$ in region of $U \geqslant 3.46$ km s^{-1}. Arrow shows location of kink in $D-U$ data.

Already when analyzing the data [17, 18, 40], a change in the form of the $D-U$ dependence at $U \geqslant 3.46$ km s^{-1} ($P \approx 20-30$ GPa) was observed, indicating an increase in the compressibility of shock-compressed liquid argon. This observation allowed us to assume the influence of ionization on the compressibility of argon under the simultaneous influence of temperature and pressure. The role of thermal action was taken into account in [40] based on the theory of free electrons in the form of the contribution to the free

energy:

$$F_e = \frac{4kT(n_p n_n)^{1/2}}{\rho} \frac{(2\pi m^* kT)^{3/2}}{h^2} \exp\left(-\frac{E}{kT}\right), \qquad (2.4)$$

where m^* is the geometric mean of the effective masses of an electron and a hole; k and h are the Boltzmann and Planck constants; n_p and n_n are the orbital degeneracy in the bands; and E is the energy gap between the valence band and the conduction band.

The behavior of the energy gap as a function of density was estimated based on the description of the entire set of experimental data; as an analysis [40] showed, the shock adiabat of argon up to 100 GPa is insensitive to the specific form of the dependence $E-\rho$. Taking into account the value of the speed of sound on the saturation line, all the $D-U$ data available at that time were approximated by the authors by two dependences:

$$D = 0.971 + 1.922U - 0.079U^2 \text{ in the area of } U \leqslant 3.46 \text{ km s}^{-1}, \qquad (2.5)$$

$$D = 2.8092 + 1.1339U \text{ in the area of } U \geqslant 3.46 \text{ km s}^{-1}. \qquad (2.6)$$

Here and below, in the regression equations of the form $D = a + bU$ or $D = a + bU + cU^2$, the values of D and U have the dimension [km s^{-1}], b are dimensionless, and c is measured in [(km s^{-1})$^{-1}$] units. The inset to Fig. 3 shows the deviation of the experimental values of the shock wave velocity D in liquid argon from the approximation dependence (2.6) in the region of $U \geqslant 3.46$ km s^{-1}.

Experimental data on the compressibility of liquid argon in coordinates $P-\rho$ are displayed in Fig. 4a up to 160 GPa in comparison with calculations using VNIIEF's EOS [40] and the universal SAHA-IV code [41].

As can be seen from the figure, the 'cold' (*1*) isotherm $T = 300$ K calculated in [40] is in good agreement with the isothermal data [21]. The Hugoniot adiabat (*2*) without taking into account ionization is consistent with the experiment up to 40 GPa, while the shock adiabat (*3*), taking into account the thermal excitation of electrons, describes the set of experimental $P-\rho$ data up to 80 GPa.

Two models of the EOS of argon, LEOS 181 [33], obtained by the quantum molecular dynamics (QMD) method, and SESAME 5173 [56], show satisfactory agreement with the experimental data in a wide range of parameters (Fig. 4b), but tend to predict higher compressibility up to 800 GPa than the experimental data. Above this pressure, both models exhibit greater rigidity. Using the linear $D-U$ dependence (2.6), we construct here the EOS of argon up to 1000 GPa (in the density range above 3 g cm^{-3}) in the Mie–Grüneisen form with the parameters $\rho_0 = 1.4$ g cm^{-3}, $c_0 = 3.25$ km s^{-1}, $n = 2.577$, $h_\Gamma = 6.45$, where ρ_0 is the initial density, c_0 is the speed of sound, n is the polytropic index, and $h_\Gamma = 1 + 2\Gamma$ is the ultimate compression ratio (where Γ is the Grüneisen coefficient). The $P-\rho$ dependence (b) calculated from this EOS virtually coincides with the calculation (*7*) based on the approximation (2.6).

The compressibility of liquid argon in the reflected shock wave was measured in the VNIIEF [40,41] and SNL [33] experiments up to 531 GPa and 900 GPa, respectively. All the results on the double compressibility of liquid argon to date are presented in Fig. 5 and are in good agreement with the VNIIEF [40, 41] and SNL [33] data in the pressure range studied. The Hugoniot adiabats *1* and *2*, calculated using EOS 5173 and LEOS 181, respectively, were taken from [33]. The dashed-dotted lines *3* and *4* present the final states in the reflected shock wave, showing slightly different agreement with the experimental data: the calculation according to EOS 5173 (blue dashed-dotted line *3*) agrees well with the data up to 800 GPa; however, above this value, the agreement of the data with the calculation according to LEOS 181 (red dashed-dotted line *4*) is better. We also note the qualitative agreement of the repeated shock calculations from [33] with the data and calculation (line *5*) in the low-pressure region from [17].

Studies of the shock compressibility of liquid argon (Fig. 4a) showed a significant effect of thermal ionization of argon atoms at a pressure of $P \approx 40$ GPa, which can be interpreted as an electronic phase transition leading to an increase in compressibility and a decrease in the temperature increase rate (see below). The studies did not reveal any other anomalies in the behavior of argon in the high-pressure and high-temperature region.

Liquid xenon. Xenon, whose band gap is the narrowest among all noble gases, is the most promising substance for

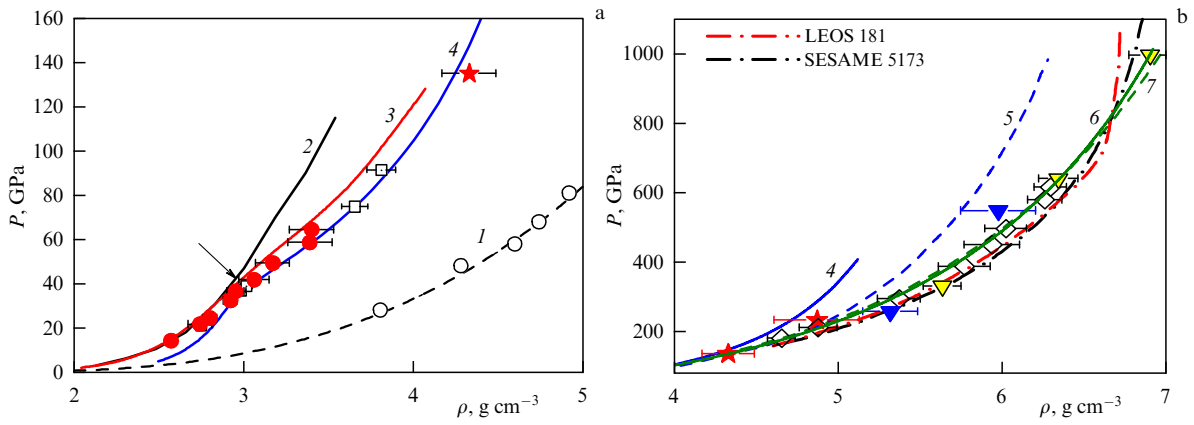

Figure 4. Dependence of pressure in shock-compressed liquid argon on density. Experiment: white squares [22, 23], red dots — [40], red stars — [41], blue triangles, white diamonds, and yellow triangles — [33]; isothermal compression $T = 300$ K: white dots — [21]. Calculation [40]: *1* — isotherm $T = 300$ K, *2* — VNIIEF EOS without taking into account electron excitation, *3* — taking into account electron excitation, *4* — calculation using SAHA-IV model [41], *5* — SESAME calculation [56], *6* — using approximation (2.6), *7* — calculation using EOS in the Mie–Grüneisen form with parameters $\rho_0 = 1.4$ g cm^{-3}, $c_0 = 3.25$ km s^{-1}, $n = 2.577$, $h_\Gamma = 6.45$. Arrow in panel indicates kink in $P-\rho$ data [40, 41].

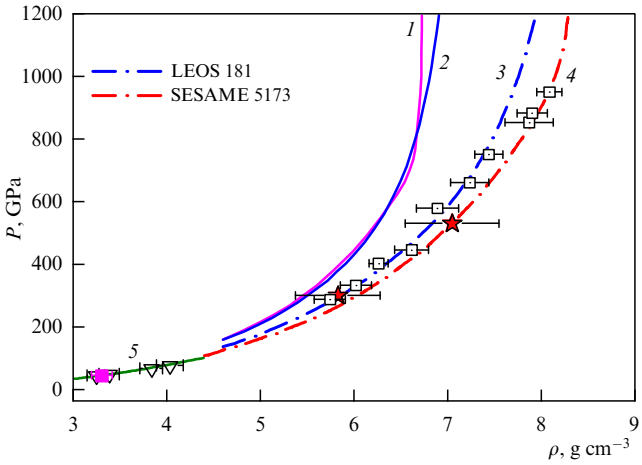

Figure 5. Compressibility of liquid argon in reflected shock wave. Experiment: white triangles — [17], white squares — [33], pink square — [40], red asterisks — [41]. Calculation [33]: *1* — shock adiabat according to LEOS 181 model, *2* — shock adiabat according to SESAME 5173 model; reflected adiabats: *3* — LEOS 181 model, *4* — SESAME 5173 model, *5* — calculation [17].

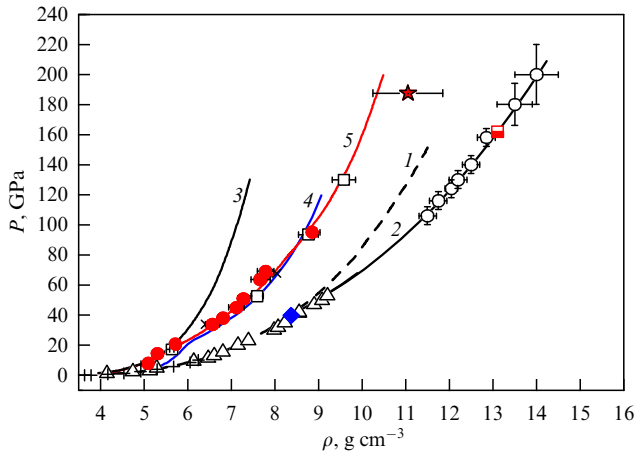

Figure 7. Hugoniot adiabat of liquid xenon. Experiment — on main adiabatic curve: white squares — [24], red dots — [42, 43], red star — [44]. Static compression: + — [68], white triangles — [69], white dots — [73]. Approximations: *1* — according to data [68, 69], *2* — according to data [73]. Calculation [42, 43]: *3* — without taking into account electron excitation (Xe1); *4* — taking into account excitation and phase transition (Xe2); blue diamond — phase transition ($\rho = 8.37$ g cm^{-3}), white and red square — metallization; *5* — SAHA-IV model [9].

searching for possible anomalies at high pressures and temperatures. The compressibility of liquid xenon in the wake of a plane shock wave in the pressure range up to 130 GPa was investigated in [24]. In VNIIEF experiments with flat and hemispherical SWGs, in addition to compressibility, the temperature at the shock wave front and electrical conductivity (see below) up to 350 GPa were measured [42–44]. In experiments using the Z-pulse accelerator, the range of xenon compressibility studies was extended to $P \approx 850$ GPa [34, 35]. All the results of experiments on the shock compressibility of xenon currently known to the authors are displayed in $D-U$ coordinates in Fig. 6a. The linear approximation of $D-U$ data in the region of mass velocities of $1.5 \leqslant U \leqslant 16$ km s^{-1} is also shown there:

$$D = (1.610 \pm 0.022) + (1.164 \pm 0.003)U\,. \qquad (2.7)$$

Figure 6b shows the deviation of the measured values of the shock wave velocity from the approximation results.

Experimental data on the compressibility of xenon in $P-\rho$ coordinates are shown in Fig. 7. To describe the data available in the 1990s, two semi-empirical versions of the EOS of xenon in the solid and liquid phases were constructed at VNIIEF: EOSXe1 and EOSXe2 [42, 43]. The Xe1 EOS model, taking into account the thermal ionization of xenon atoms, described well the data on the pressure and temperature of shock compression up to 20–25 GPa and quasi-isentropic compression up to 40 GPa, but failed to describe the results at higher pressures. This anomaly, along with the data on the isothermal compressibility of xenon examined in [68–73], necessitated development of a new model of a more closely packed phase of xenon. X-ray structural analysis of compressed xenon on the isotherm $T_0 = 300$ K in the studies cited above revealed a transition of the initial face-centered cubic (FCC) lattice of xenon above 75 GPa to a hexagonal close packed structure (HCP), the closing of the energy gap at a density of 12.3 g cm^{-3} and a pressure of 132 GPa, and an anomaly in the absorption spectrum of radiation at 150 GPa, which was associated with the transition to the metallic state. Taking into account the approximations of the data in [68–73], presented in Fig. 7 (curves *1* and *2*), it was hypothesized in [42, 43] that, in compressed xenon at a density of

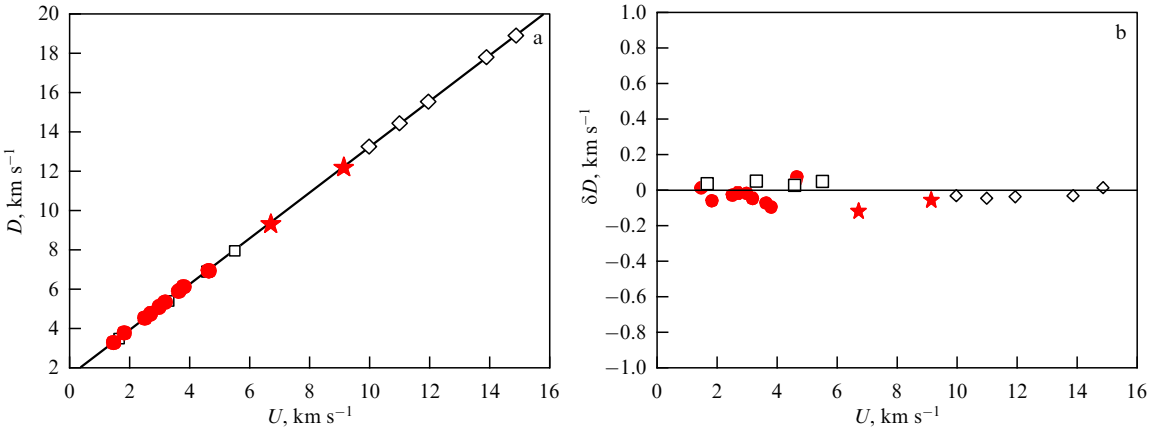

Figure 6. Hugoniot adiabat of liquid xenon. Experiment: red dots — flat SWG [42, 43], white squares — [24], red stars — hemispherical SWG [44], white diamonds — [34, 35]. Solid black line — linear approximation of data (2.7).

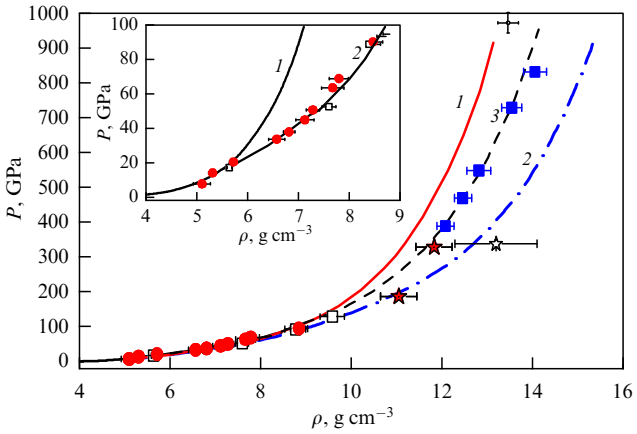

Figure 8. Dependence of pressure in shock-compressed liquid xenon on density. On main adiabat: white square — [24], red dots — [42, 43], red stars — [44], blue squares — [34]; white star — on reflected adiabat [44]. Calculation: *1* — using approximation (2.7), *2* — LEOS540 [34], *3* — SESAME5191 [34]. In inset [42, 43]: *1* — calculation without taking into account excitation of electrons from valence band to conduction band, *2* — calculation taking into account excitation.

$\rho = 8.37$ g cm^{-3}, a structural transition occurs (blue diamond in Fig. 7) without a density jump and the energy gap closes, characterizing metallization, at a density of $\rho = 13.13$ g cm^{-3} (white and red square in Fig. 7). It was believed that during the phase transition only a change in the slope of the elastic interaction curve occurs. The new Xe2 EOS described well in a unified way all the data available at that time, including those on shock wave compressibility up to 70 GPa (curve *4* in Fig. 7), on the temperature at the shock wave front up to 15 kK, and on electrical conductivity up to 1.2×10^3 Ω^{-1} cm^{-1} (see below).

In the pressure range up to $P \approx 90$ GPa, the experimental data on xenon compressibility are also in satisfactory agreement with the calculation made using the SAHA-IV model [9].

The VNIIEF data [42–44] on the shock-wave compressibility of liquid xenon, together with the results of [34, 35], presented in Fig. 8, at pressures above 200 GPa exhibit a significant difference from the calculations [34] that use the EOS xenon models — SESAME 5190 (curve *1*) and LEOS 540 (curve *2*). By combining the experimental data in [34], a multiphase EOS 5191 was developed, which can describe the properties of xenon in a wide range of pressures and temperatures (curve *3*, Fig. 8). In the inset in Fig. 8, the role of thermal ionization of xenon atoms during shock compression is convincingly shown — the calculation that does not take it into account (curve *1*) agrees with the data only up to 20 GPa.

Liquid krypton. Among all the noble gases, the properties of krypton at high pressures and temperatures have been the least studied. In the 1990s, the properties of liquid krypton such as compressibility, temperature, and electrical conductivity were studied in the most complete way at VNIIEF up to 90 GPa in experiments with a flat SWG [45]; almost 25 years later, the studied range was extended to 200 GPa in experiments with a hemispherical SWG [46]. Almost concurrently, the compressibility of krypton up to 850 GPa was measured in [36]. All currently known experimental $D-U$ data on the compressibility of liquid krypton are presented in Fig. 9a; in the region of mass velocities of $2.0 \leqslant U \leqslant 16.5$ km s^{-1}, they are approximated by a straight line:

$$D = (1.820 \pm 0.0444) + (1.193 \pm 0.005)U\,. \qquad (2.8)$$

Experimental data on the compressibility of krypton on the Hugoniot adiabat in $P-\rho$ coordinates are displayed in Fig. 10 together with the calculation results.

It is evident from Fig. 10 that the best description of all data on the first SW is provided by the LEOS Y360 model [36], which, in the pressure range up to $P \approx 600$ GPa, virtually coincides with the dependence calculated using approximation (2.8). Up to $P \approx 400$ GPa, the experimental data are in good agreement with the calculation made using the SESAME 5181 model. The inset to Fig. 10 in the pressure range up to $P = 100$ GPa shows good agreement between the experimental data and the calculation made using the modified SAHA model [46]. The experimental data differ most significantly from the calculation using the LEOS 360 model.

For practical gas-dynamic calculations of states in krypton, it is convenient to use the Mie–Grüneisen EOS with the parameters $\rho_0 = 2.42$ g cm^{-3}, $c_0 = 1.92$ km s^{-1}, $n = 3.101$, $h_\Gamma = 5.382$ selected using approximation (2.8). The root-mean-square error of the pressure values calculated using the Mie–Grüneisen EOS with the given parameters for the pressures using approximation (2.8) is 0.243%.

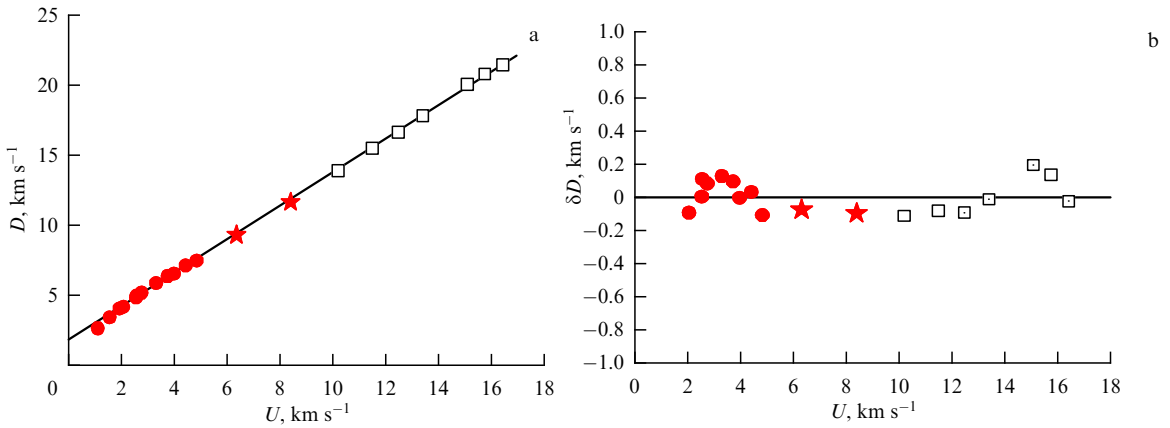

Figure 9. (a) Hugoniot adiabat of liquid krypton. Experiment: red dots — [45], red stars — [46], white squares — [36]; (b) deviation of experimental values of SW velocity from approximation (2.8).

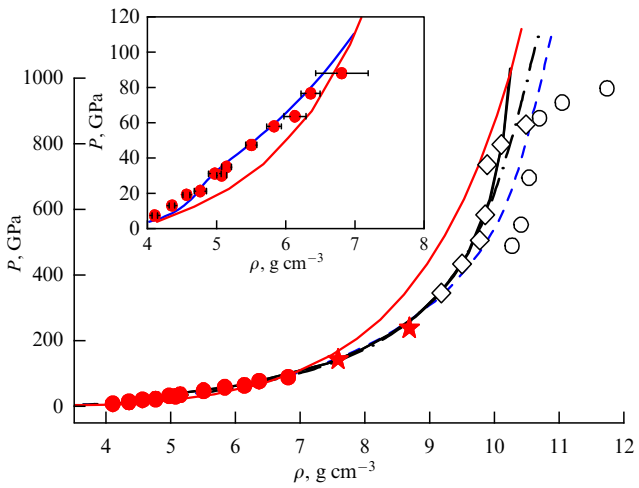

Figure 10. Dependence of pressure in shock-compressed liquid krypton on density. Experiment: red dots — [45], red stars — [46], white diamonds on direct wave and white dots on reflected wave — [36]. Calculation [36]: black dashed-dotted line — LEOSY360, red solid line — LEOS360, blue dashed line — SESAME5181; black solid line — Hugoniot adiabat calculated using approximation (2.8). Inset: experimental data in pressure range up to $P \approx 100$ GPa [45]. Calculation: blue line — modified SAHA model [46], red line — calculation using LEOS360.

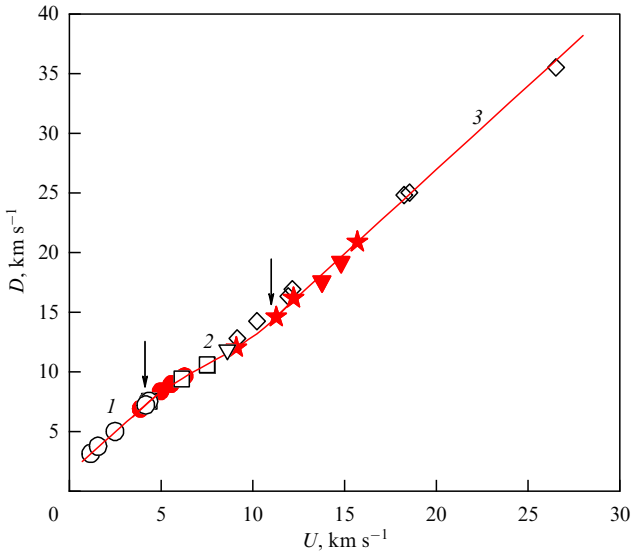

Figure 11. Shock adiabat of nitrogen. Experiment: white dots — [25], white triangle — [30], white squares — [17], white diamonds — [37], red dots — [47], red stars — [47], red triangles — [49]. Approximation [47] (solid red line): in region *1* — $D = 1.572 + 1.365U$ (1 km s^{-1} < U < 4.17 km s^{-1}), in region *2* — $D = -2.008 + 3.375U - 0.337U^2 + 0.015U^3$ (4.17 km s^{-1} < U < 11.3 km s^{-1}), in region *3* — $D = 1.174 + 1.407U$ ($U \geqslant 11.3$ km s^{-1}).

Liquid nitrogen. Studies of the properties of nitrogen, due to its cosmological abundance and ability to form numerous chemical compounds at high pressures and temperatures, are of interest for the physics of condensed matter, the internal structure of planets, and chemical explosives. V.N. Zubarev and G.S. Telegin were the first to study the compression of liquid nitrogen in the wake of a plane shock wave up to 40 GPa at VNIIEF [25]. The compressibility, temperature, and electrical conductivity of shock-compressed liquid nitrogen were measured up to 260 GPa at VNIIEF using generators of plane and hemispherical shock waves [47]. In study [48], liquid nitrogen was compressed to a density of $\rho \approx 3.25$ g cm^{-3} under a pressure of 325 GPa. American researchers in the range of pressures of 20–110 GPa measured the compression of liquid nitrogen to a density of 3.5 g cm^{-3}, a temperature in the range of 4000–14,000 K, and an electrical conductivity of up to 50 Ω^{-1} cm^{-1} [27–30]; a Z-pulsed accelerator was used to extend the research to 840 GPa [37]. The VNIIEF results [25, 47, 48] and the data [27–30] in $D-U$ coordinates, shown in Fig. 11, were approximated more than 12 years ago in [46] by a dependence (solid red line in Fig. 11), consisting of three piecewise smooth segments (see figure captions) for various intervals of change in mass velocity.

In 2022, two new studies, [37] and [49], were reported which investigated the properties of shock-compressed nitrogen in the megabar pressure range. The first one [37] conducted shock experiments at the Omega laser facility with liquid nitrogen pre-compressed in diamond and sapphire anvil cells to an initial pressure of 0.23–2.03 GPa and an initial density in the range of 0.76–1.29 g cm^{-3}. In the second study [49], carried out at VNIIEF, shock-wave compression of gaseous nitrogen with a density close to that of the liquid was investigated in hemispherical high-pressure devices [74], previously used at VNIIEF in experiments with deuterium and helium [75, 76]. Figure 11 shows that the results obtained in the new VNIIEF experiments [49] (red triangle) are in good agreement with the data from [25, 27–30, 47, 48]. In the further analysis presented below, we only consider the data from [37], presented in Fig. 11, for initial densities in the range of 0.756–0.863 g cm^{-3}. This range of nitrogen densities also includes the states of nitrogen ($\rho_0 = 0.807$ g cm^{-3}) explored in the experiments in [25, 27–30, 47, 48]. As can be seen from Fig. 11, the data from [37] in the region of mass velocities of $U \geqslant 13$ km s^{-1} are well described by approximation 3 from [47]. The difference between the $D-U$ results of [37] and the VNIIEF data only occurs in the range of mass velocities of 9–15 km s^{-1}; the plausible reasons for this will be analyzed below.

The $P-\rho$ data [25, 27–30, 47, 48] and those of SNL [37] for experiments in the range of initial densities of liquid nitrogen of 0.756–0.863 g cm^{-1} are compared in Fig. 12. Similar to the $D-U$ dependence (see Fig. 11), three regions can be distinguished in Fig. 12 with different behaviors of the $P-\rho$ dependences. The region of relatively low pressures ($P \leqslant 50$ GPa) of shock compression of molecular nitrogen is replaced by a region of an intermediate pressure range (50 GPa $\leqslant P \leqslant$ 100 GPa) with a relatively low slope of the $P-\rho$ dependence, apparently corresponding to the polymer structure of a dense nitrogen fluid (indicated by arrows), and, finally, in the high-pressure region ($P >$ 100 GPa), the $P-\rho$ dependence on the shock adiabat changes its character sharply to become close to the limiting value of compression for a monatomic ideal gas: $\rho/\rho_0 \approx 4$. This behavior of the shock adiabat, first observed in [47], indicates the existence of a fairly extensive zone of nitrogen plasma parameters with an almost constant value of the Grüneisen parameter $\mathrm{Gr} \equiv (\partial PV/\partial E)_V \approx 0.62$. Based on the analysis of a set of experimental and theoretical data, the following conclusion was made in [47]: the pressure range $P \approx 100$ GPa and higher corresponds to the end of the depolymerization process.

An increase in the compressibility of liquid nitrogen at pressures above 30 GPa (softening of the $P-\rho$ curve) and its decrease (increased rigidity of the $P-\rho$ curve) at pressures above 60 GPa were noted earlier in [28–30]. Experiments have

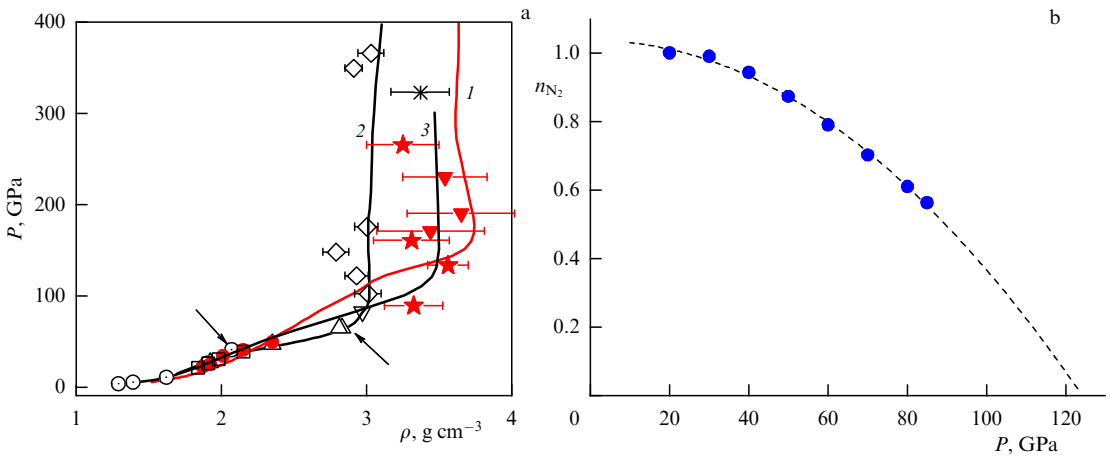

Figure 12. (a) Dependence of pressure in nitrogen plasma on density. Experiment: white dots — [25], white diamonds — [37], white triangles (△) — [17], white squares, white triangles (▽) — [30], red dots, red stars — [47], red triangles — [49], ✳ — [48]. Calculation: *1* — SAHA-N model [47], 2 — DFTMD [37], *3* — compressible covolume model [48]. Arrows indicate boundaries of polymer phase of nitrogen. (b) Dependence of concentration of nitrogen molecules on pressure: blue dots — calculation, dashed line — approximation.

shown that, for a fixed specific volume, the temperature of doubly compressed nitrogen turned out to be lower than that on the main shock wave, while the ratio between the pressures of doubly and singly compressed gas is the inverse. It is easy to estimate that in this case the internal energy in the states behind the reflected wave is less than behind the main one, i.e., in an isochoric process, an increase in pressure leads to a drop in the internal energy.

Since

$$\left(\frac{\partial E}{\partial P}\right)_V = C_V\left(\frac{\partial P}{\partial T}\right)_V^{-1} = -C_V\left(\frac{\partial V}{\partial T}\right)_P\left(\frac{\partial V}{\partial P}\right)_T^{-1} < 0\,,$$

it follows from experiments with the reflected wave that the derivative $(\partial P/\partial T)_V$ becomes negative. This is possible with the loss of mechanical stability of the molecular phase $(\partial P/\partial V)_T > 0$, or with a negative thermal expansion coefficient $\beta_T = -(1/V)(\partial V/\partial T)_P < 0$. The unusual results obtained were evidence of the first discovered shock-induced cooling associated with the onset of the dissociation process of the N_2 molecule. This conclusion about the dissociation of molecular nitrogen into an atomic liquid is in line with the data obtained in [37], as can be seen from Fig. 12. However, the results of experiments and modeling [37] for initial nitrogen densities of 0.756–0.863 g cm^{-3}, presented in Fig. 12, predict an earlier onset of the nitrogen dissociation process than do the VNIIEF results [47–49]. The most likely reason for this is the geometric dimensions of the nitrogen samples studied. With a nitrogen layer thickness of $\sim (100-200)$ μm and impact velocities $D \sim 10-35$ km s^{-1} in [37], the time that nitrogen remains in the compressed state is $\Delta t \sim 10-30$ ns, while in the VNIIEF experiments the nitrogen layer thickness is ~ 4000 μm and the time of the compressed state is $\Delta t \sim 250-300$ ns. Under such loading conditions, the relaxation effect of the process comes to the fore: in microscopic objects [37], relaxation does not have time to complete during the compression time and a partial transformation process is realized, while under the conditions of macroscopic VNIIEF objects [47–49], it does. Indeed, in the region of the onset of the anomaly, the temperature values reach the dissociation limit, and the dissociation reaction can form a channel for phase transformation. The kinetics of a process of this kind were considered in [77], where the estimated barrier for a dissociation of several electron volts was obtained, and it was shown that a reaction time decreases with increasing pressure from several microseconds to several nanoseconds. The dependence of the degree of dissociation of nitrogen molecules calculated in [77] is shown in Fig. 12b. The approximation of the calculated data suggests that, at a pressure of 100 GPa, $\sim 60\,\%$ of the N_2 molecules are dissociated, while for complete dissociation, the pressure must exceed 120 GPa.

The authors state that, as a result of experiments conducted in various laboratories around the world, a database is now available on the compressibility of micro- and macroscopic nitrogen samples in the pressure range up to 1400 GPa with times of nitrogen plasma maintained in the compressed state from 10 to 300 ns. The data obtained do not disagree with each other and enable a more accurate determination of how the change in the transformation mechanism is associated with the transformation of loading conditions. The DFT modeling used in [37] assumes an instantaneous nature of the transformations, which is possibly an incorrect approximation for describing macroscopic objects in the VNIIEF experiments. Despite the large amount of experimental material accumulated to date in the study of the properties of liquid nitrogen, it has not yet been possible to fully explain the features of its behavior.

3. Speed of sound and Grüneisen coefficients

The main parameters of a shock wave — its velocity D and the mass velocity of particles U — determine the state of the shock-compressed substance, its density ρ, and pressure $P = \rho_0 DU$. Another important parameter of the shock-compressed state is the speed of sound C, with which small perturbations propagate in the wake of the shock wave front. Knowledge of the speed of sound is necessary for the correct design of an experiment on the compressibility of materials, for testing equations of state, and for solving various problems in geophysics. Since $C + U > D$ [78, 79], any perturbation that occurs behind the shock wave front catches up with the front and affects its amplitude. This circumstance makes it possible to measure the speed of propagation of sound perturbations, recording the moment it reaches the SW front.

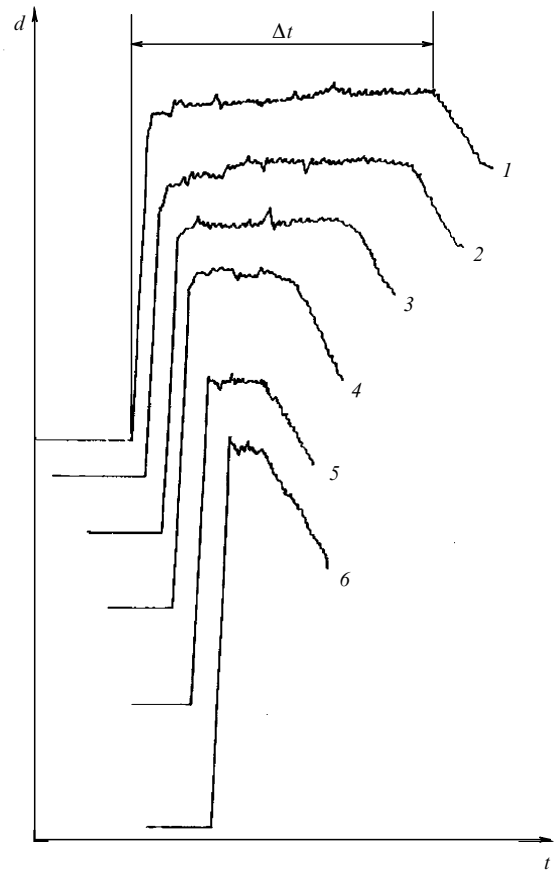

Figure 13. Densitograms of radiation of shock wave front in liquid krypton at various shock compression pressures (d — blackening density of photographic film).

The first methods for recording the speed of sound behind the front of powerful shock waves, which were developed in the late 1940s, were called the 'lateral' and 'catch-up' unloading methods [78, 79]. The simplest way to measure the speed of sound in liquefied inert gases is the 'catch-up' unloading method in combination with optical recording of the shock wave front glow. The main advantage of the method is the high sensitivity of the dependence of the shock wave front glow on its amplitude, which makes it possible to detect very small variations in pressure. The authors of [80] were the first to point out that the speed of sound can be measured using this method. The data on the speed of sound are used as an additional factor for testing the EOS parameters of the studied substances.

Values of the speed of sound up to 8 km s^{-1} and the Grüneisen coefficients in argon, krypton, xenon, and nitrogen were measured at VNIIEF concurrently with temperature and compressibility in the design displayed in Fig. 1. The thickness of the cryogenic liquid layer was $\sim 10-15$ mm, so that the unloading wave could definitely catch up with the shock wave front in the sample thickness. Figure 13 shows a series of typical densitograms (liquid krypton) at various shock compression pressures ($P_1 < P_2 \ldots < P_6$), where one can clearly see the drop in radiation intensity due to the decrease in shock compression pressure associated with the 'catching up' of the shock wave front by the unloading wave.

The catch-up time values Δt were measured directly using photometry results. By computer modeling of these experiments using the program [60], the values of the speed of sound in the studied substances were obtained with known kinematic parameters for the striker, screen, and sample. When making calculations for the materials of the strikers and screens, their equations of state from the VNIIEF library were used. Analysis shows that the values of the speed of sound were determined by this method with an accuracy of $\approx 10\%$. The obtained data on the speed of sound for argon, krypton, and xenon are presented in Fig. 14a. The dependence of the speed of sound in shock-compressed liquid nitrogen on the shock wave amplitude is shown in Fig. 14b. The figure also presents dependences approximating the experimental data: for argon $C(P) = (3.968 \pm 0.152) + (0.054 \pm 0.004)P$; for krypton $C(P) = (2.981 \pm 0.113) + (0.029 \pm 0.002)P$; and for xenon $C(P) = (2.864 \pm 0.165) + (0.023 \pm 0.003)P$, where $[P]$ — GPa, $[C]$ — km s^{-1}.

The Grüneisen coefficient Γ is directly related to the speed of sound and the Hugoniot adiabat (see, for example, [82])

$$C^2 = -V^2 \frac{\mathrm{d}P}{\mathrm{d}V}\left[1 - \frac{(\Gamma/V)(V-V_0)}{2}\right] + V^2\left[\frac{(\Gamma/V)(P_\mathrm{n}-P_0)}{2}\right] + V^2(P-P_\mathrm{n})\left[\frac{\Gamma}{V} + \frac{\mathrm{d}\ln V/\gamma}{\mathrm{d}V}\right]. \quad (3.1)$$

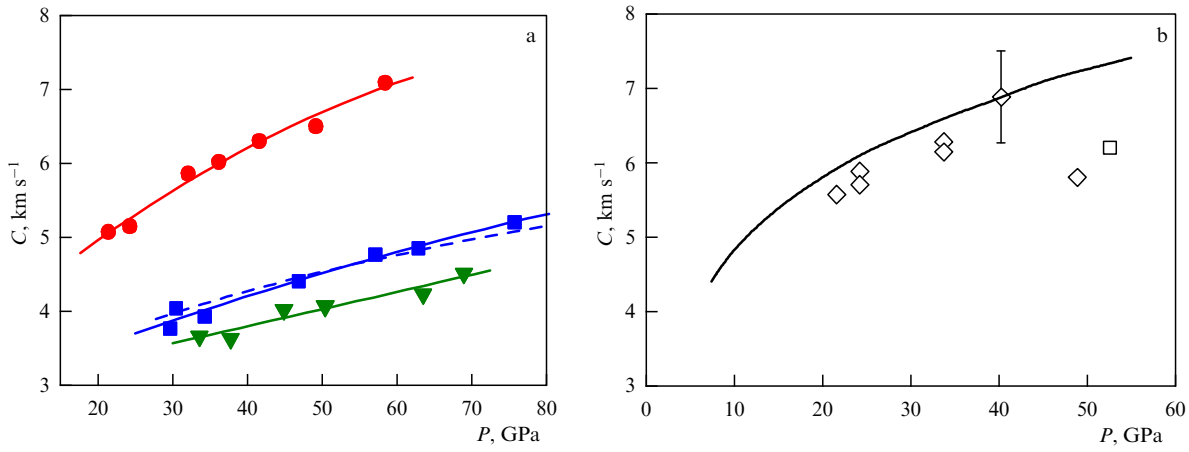

Figure 14. Dependence of speed of sound on pressure: (a) red dots — argon [40], blue squares — krypton — [45], green triangles — xenon (this study), solid lines — approximations, blue dashed line — calculation [81]; (b) liquid nitrogen: white diamonds — this study, white square — [30]. Solid line — calculation by A.B. Medvedev (private communication).

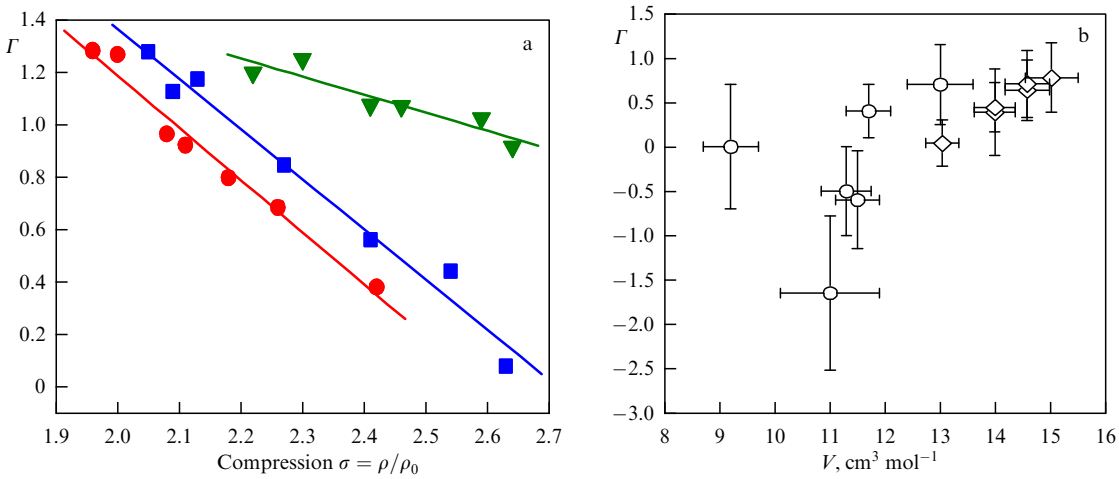

Figure 15. (a) Dependence of Grüneisen coefficient on degree of compression: green triangle — xenon (this study), red dots — argon [40], blue squares — krypton [45], solid lines — approximations; (b) nitrogen: white dots — [30], white diamonds — this study.

Here, V and V_0 are the specific volumes in the compressed and initial states, P_n is the pressure on the shock adiabat, and P is the pressure on the isentrope. The first two terms in Eqn (3.1) describe the speed of sound on the Hugoniot adiabat, while the last one presents the dependence of the speed of sound on the pressure when moving away from the Hugoniot adiabat. If the speed of sound and the shock adiabat of a substance are determined in independent experiments, the Grüneisen coefficients can be found from Eqn (3.1). Indeed, for $P = P_n$, we have

$$\Gamma = \frac{\left[C^2 + V^2\,\mathrm{d}P/\mathrm{d}V\right]}{\left\{V\left[(\mathrm{d}P/\mathrm{d}V)(V_0 - V)/2 + P/2\right]\right\}}\,. \tag{3.2}$$

The dependences of the Grüneisen coefficients on the compression ratio for liquefied noble gases and nitrogen are displayed in Fig. 15. For xenon, the values of Γ are shifted in compression by +0.5.

Depending on the degree of compression $\sigma = \rho/\rho_0$ (where ρ and ρ_0 are the final and initial densities of the substance), the calculated values of the Grüneisen coefficient Γ are approximated by the following dependences: for krypton — $\Gamma(\sigma) = (5.188 \pm 0.301) - (1.912 \pm 0.130)\sigma$; for xenon — $\Gamma(\sigma) = (2.767 \pm 0.337) - (0.690 \pm 0.138)\sigma$; and for argon — $\Gamma(\sigma) = (5.165 \pm 0.303) - (1.990 \pm 0.141)\sigma$.

4. Temperature, absorption, and reflection of light in shock-compressed liquefied noble gases and nitrogen

The system of Eqns (2.1) (Section 2) does not include temperature, which is one of the main thermodynamic characteristics of the state of matter. By selecting coefficients and functions (in a particular EOS version), it is possible to satisfactorily describe the compressibility and pressure measured in the experiment; however, the shock compression temperature in various calculation options is very sensitive to both the choice of the equation of state itself and the assumptions regarding the coefficients included in it. Under such conditions, the experimental measurement of temperatures in shock-wave experiments allows one to reliably substantiate the chosen form of the equation of state and enables independent verification of its parameters, in particular, the behavior of heat capacity under high compression. This type of thermodynamic information often turns out to be a much more sensitive means of verifying theoretical models than the Hugoniot adiabat alone. Simultaneous measurement of compressibility and temperature in an experiment allows one to obtain more complete thermodynamic information about the state of a shock-compressed substance, which is of importance for substantiating the form of the equation of state.

Studies of the radiative properties of shock wave fronts in many condensed materials are limited by their opacity. However, for transparent media, there are no obstacles to recording the spectral brightness of the shock front glow, by which its temperature is estimated, through a layer of not yet compressed substance using optical methods. Taking into account the extremely small thickness of the shock front, the measured temperatures are usually related to the temperatures of the substance behind the shock front. For such temperature measurements with good time resolution under conditions of a fast process in the shock wave ($t \sim 10^{-6} \ldots 10^{-7}$ s), highly sensitive and low-inertia optical methods, based on the temperature dependence of the body's radiation, are usually applied.

The main relationship between the radiation and temperature of an absolutely black body (BB) is described by the Planck function:

$$N(\lambda) = \mathcal{E} C_1 \lambda^{-5}\left[\exp\left(\frac{C_2}{\lambda T}\right) - 1\right]^{-1} = C_1 \lambda^{-5}\left[\exp\left(\frac{C_2}{\lambda T_s}\right) - 1\right]^{-1}. \tag{4.1}$$

Here, $\mathcal{E}$ is the emissive capacity of the body, λ is the wavelength, T is the true temperature, and T_s is the brightness (spectral) temperature; the constants $C_1 = 1.19 \times 10^{-16}$ W m^2 sr^{-1} and $C_2 = 0.0144$ m K.

In practical studies of shock-compressed materials, the method of measuring brightness temperatures is used most widely. The introduction of brightness temperature into optical pyrometry makes unnecessary determining the absorptivity of the emitting body in experiments. In this method, the absolute value of the emissive capacity of the body is not measured but is compared with the emissive capacity of a reference black body with a known value of the

brightness temperature, T_s. The brightness (T_s) is the temperature of a BB that has the same monochromatic brightness at a selected wavelength as the body under study with a temperature T, i.e.,

$$N_0(\lambda, T_s) = N(\lambda, T) = \mathcal{E}(\lambda, T) N_0(\lambda, T)\,. \qquad (4.2)$$

The technique for measuring the brightness temperatures of the shock wave front in air and noble gases was first proposed in [83, 84]. A large amount of experimental data on the emissive capacity of shock waves in dense gases is reported in [85]. The technique for studying the emissive capacity of shock waves in condensed dielectrics was further developed at the VNIIEF in studies by S.B. Kormer, G.A. Kirillov, and M.V. Sinitsyn [80, 86–89], which convincingly showed that the temperatures of transparent condensed shock-compressed substances can be measured using their thermal radiation.

The brightness temperatures at the shock wave front in liquid argon and nitrogen up to 20 GPa were measured for the first time by I.M. Voskoboinikov, A.Yu. Dolgoborodov, and M.F. Gogulya [26]. The VNIIEF results extended the research on the temperatures of shock-compressed liquefied gases to pressures of 265 GPa in nitrogen [47], up to 100 GPa in krypton [45, 46], and up to 350 GPa in argon [40, 41] and xenon [42–44]. The temperature of shock-compressed liquid nitrogen and xenon was also studied in [30, 49] and [90, 91], respectively.

In the VNIIEF experiments, either an optical system (Fig. 1a) or a quartz fiber light guide (see Fig. 2) was used to transmit radiation from the SW front to the recording equipment. The brightness temperatures were determined based on the experimental results using the actinic flux method [86]. The actinic flux A acting on the photographic layer can be represented as

$$A = \int_{\lambda_1}^{\lambda_2} N(\lambda) S_\lambda \tau_\lambda \, \mathrm{d}\lambda\,, \qquad (4.3)$$

where S_λ is the spectral sensitivity of the photographic layer, τ_λ is the transmittance of the light filter, and $N(\lambda)$ is the spectral brightness of the photographic light source (4.1). The integration limits λ_1 and λ_2 are determined by the transmittance boundaries of the selective light filter and the spectral sensitivity of the photographic film. When neutral light filters were used in the experiments, the dependence of their transmittance on temperature was taken into account.

For experiments on measuring the temperature and light absorption coefficients with high time resolution, a high-speed electron-optical pyrometer [59] with five channels for recording radiation at wavelengths $\lambda = 406$, 450, 498, 550, and 600 nm, selected by interference filters with a maximum radiation transmission of $\approx 50\%$ with a bandwidth of 10 nm at half maximum, was used. Photomultiplier tubes (PMs) with an anode current rise rate of 1.2 ns were used to record radiation pulses. A pulse lamp [92] calibrated against a standard incandescent ribbon lamp was used to calibrate the optical path of the pyrometer.

In the pressure range of up to 100 GPa, the main set of experimental data was obtained using the photographic method of recording radiation in the red region of the spectrum ($\lambda = 670$ nm). The experimental scheme is presented above (Fig. 1a). The photochronograms of SW front radiation and the film blackening densitogram shown in Fig. 1b, c, respectively, are typical of experiments with liquefied gases. The brightness temperature was estimated by the film blackening density in the region of constant glow brightness (*1–2*) (Fig. 1c). The duration of this region, which is determined by the time the liquid is in the compressed state, decreases with increasing shock compression pressure. The time resolution in these experiments is determined by the size of the slit image of a high-speed photorecorder on the film and the linear scanning rate and is 1.5×10^{-7} s. When recording radiation using a multichannel pyrometer [59], the problem of determining the SW front temperature from the measured spectral temperature values was solved using the nonlinear least squares method for two parameters T and $\mathcal{E}$ (see Eqn (4.1)) and iterations to obtain accurate estimates of the temperature and emissive capacity. The error in determining the temperature and emissive capacity was estimated from the formulas

$$\delta T = \frac{\sigma_N}{(\partial N_\lambda/\partial T)_{\mathcal{E},\,\lambda=\langle\lambda\rangle}}\,, \qquad \delta\mathcal{E} = \frac{\sigma_N}{(\partial N_\lambda/\partial \mathcal{E})_{T,\,\lambda=\langle\lambda\rangle}}\,. \qquad (4.4)$$

Here, σ_N is the standard deviation for the spectral radiation flux, and the derivatives are calculated at the average value of the transmission wavelengths of all channels.

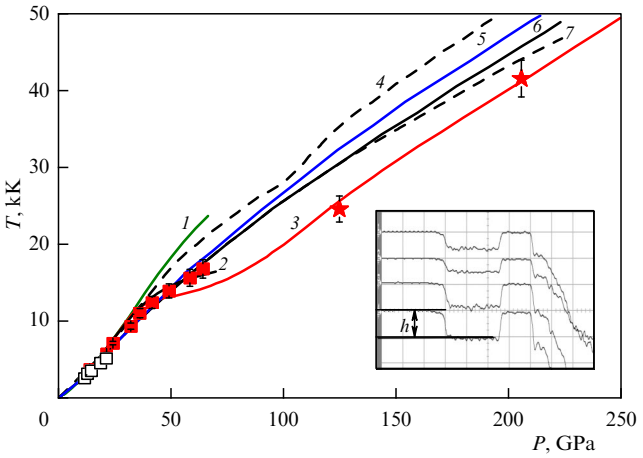

Figure 16. Dependence of temperature of shock-compressed liquid argon on pressure. Experiment: white squares — [26], red squares — [40], red stars — [41]. Calculation [40]: *1* — taking into account excitation of electrons, *2* — effective temperature in red region of spectrum ($\lambda = 670$ nm) according to Zeldovich model [88], *3* — SAHA IV model [41]. Calculation [33]: *4* — SESAME5172, *5* — LEOS 181, *6* — LEOS 180, *7* — SESAME 5173. Inset: oscillograms of SW front radiation in the experiment: wavelength (top to bottom) 550, 498, 406, 450 nm. Sweep — 100 ns/div.

Liquid argon. The experimental temperatures of shock-compressed liquid argon as a function of pressure are presented in Fig. 16 [40, 41].

The inset shows typical oscillograms of the shock wave front radiation in liquid argon. The temperature was estimated from the amplitude h of the signals. As can be seen from the oscillograms, in shock-compressed liquid argon, the maximum temperature is reached almost immediately after the SW leaves the screen. To calculate the equilibrium temperatures in argon, EOS [40] was used at VNIIEF. As was shown above, the examination of shock compression led to the discovery of electron excitation in liquid argon under the simultaneous action of high pressures and temperatures. However, the semi-empirical equation of state of argon [40], which takes into account the thermal

excitation of electrons (curve *1* in Fig. 16), fails to describe the set of experimental data in the pressure range up to 100 GPa, which indicates a higher sensitivity of temperature measurements for testing model equations of state than $D-U$ data.

Even when measuring the temperatures of shock-compressed alkali halide crystals in [86–89], a systematic lag of the measured temperatures from those calculated using the equations of state was noted starting at a temperature of $T \sim 10^4$ K. A theory explaining this phenomenon was proposed by Zeldovich et al. [88]. The theory is based on the assumption that 'cold' electrons screen radiation from deeper layers of the shock-compressed substance, where temperature equilibrium is established between the electrons and the lattice. Based on this theory, the effective temperatures in argon were calculated in [40], and good agreement between the experimental and calculated temperatures (curve *2* in Fig. 16) up to 65 GPa was shown.

The temperatures of shock-compressed liquid argon were calculated in [41] using the universal SAHA-IV code in a modified chemical plasma model, where argon was calculated as a strongly nonideal mixture of ions, electrons, and atoms. In calculating the equilibrium composition of the plasma and its thermodynamic properties, the effects of partial degeneracy of the electron component and interaction between all types of particles were taken into account. An improved modification of the pseudopotential approach was used to describe the Coulomb nonideality. The effective depth of the specified potential was set equal to the interaction energy of the electron-ion pair at an average distance between heavy particles (ions and atoms), which corresponds to the boundary energy adopted in this model separating free and bound (intra-atomic) states taken into account when calculating the atomic partition function. In addition to the contribution of the Coulomb interaction of charged particles, the effect of intense repulsion of heavy particles at close distances was taken into account. This was done using an approximate equation of state of 'soft spheres' modified for a mixture of particles of various diameters. The degree of 'softness' in the specified potential of intermolecular repulsion was selected based on the requirement of the best description of the experimentally measured equation of state of argon at room temperature. The dependence of argon temperature on pressure calculated using the SAHA-IV model (curve *3*) describes well the experimental data in the pressure range of 125–206 GPa (Fig. 16), but exhibits a decrease in the rate of temperature growth above 50 GPa.

Shock compression temperatures of argon higher than those in SAHA IV are obtained from calculations using EOS SESAME5172 (5173) and LEOS 180 (181) [33]. In the pressure range up to 250 GPa (see Fig. 16), calculations using LEOS 180 (curve *5*) and SESAME 5173 (curve *6*) are in good agreement with each other and with calculations using QMD modeling with various potentials.

Liquid xenon. The data on the temperature of shock-compressed liquid xenon obtained at VNIIEF with flat and hemispherical SWGs [42–44], together with the results of [90, 91], are presented in Fig. 17. The difference between brightness temperatures in the red (red diamonds — $\lambda = 670$ nm) and blue (blue dots — $\lambda = 430$ nm) regions of the spectrum reflects the well-known fact that quanta in the shorter-wavelength region of the spectrum feature a lower absorption coefficient and therefore emerge from deeper layers of the shock wave front, where the radiation is closer to equilibrium.

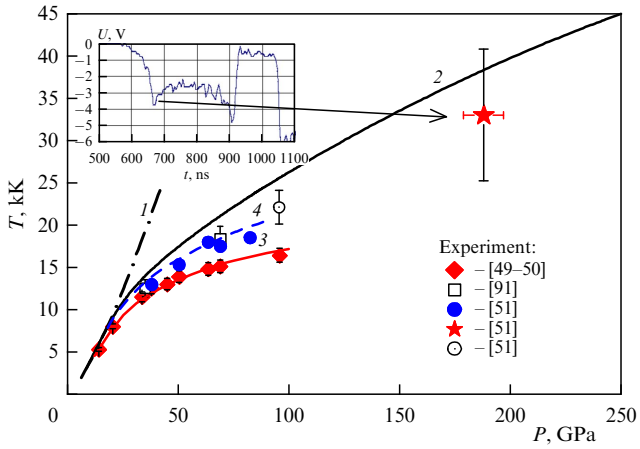

Figure 17. Temperature of shock-compressed liquid xenon as a function of pressure. Calculation [42, 43]: *1* — equilibrium temperature without electron excitation, *2* — temperature with excitation. Calculation using Zeldovich model [88]: *3* — temperature in red ($\lambda = 670$ nm) region of spectrum, *4* — temperature in blue ($\lambda = 430$ nm) region of spectrum. Inset shows oscillogram of SW front radiation in xenon at pressure $P = 188$ GPa ($\lambda = 406$ nm).

The effective temperatures calculated in [42–44] using the Zeldovich model, which takes into account the screening of radiation from the inner layers of the shock wave front by 'cold' outer electrons, describe well the experimental results in the pressure range up to 100 GPa.

In [44], a feature of the SW front radiation in xenon was observed: after a sharp increase, radiation brightness decreases as the SW moves along the sample. A characteristic oscillogram of the SW front radiation in liquid xenon in the experiment [44] at a pressure of 188 GPa is displayed in the inset to Fig. 17. Temperature was estimated from the maximum radiation intensity achieved after the shock wave exited into liquid xenon. The mechanism for reducing the temperature at the shock wave front in xenon in this pressure range is currently unknown.

Liquid krypton. In VNIIEF experiments with a flat SWG in the pressure range of 20–90 GPa, brightness temperatures of 5–20 kK in shock-compressed liquid krypton were measured [45]. In experiments with hemispherical SWGs, the radiation of the SW front in liquid krypton was recorded at five wavelengths [46]. The experimental values of the temperatures [45, 46] of shock-compressed liquid krypton as a function of pressure and density are displayed in Fig. 18. The obtained data as a function of pressure are approximated by the dependence (curve *1*)

$$T(\text{kK}) = 0.581 + 0.3308P - 4.646 \times 10^{-4}P^2\,, \qquad (4.5)$$

where $[P]$ – GPa.

The results for the temperature of shock-compressed liquid krypton in the pressure range up to 300 GPa, as can be seen from Fig. 18, are in fairly good agreement with the QMD calculations made in both [36] and [46] and the SAHA model calculation [46] together with the set of $P-\rho$ data presented above.

It is known that the law of corresponding states is fulfilled for thermodynamically similar substances, which include noble gases. Since the critical parameters are determined independently of the form of the equation of state, the law of corresponding states has a general nature. The results of

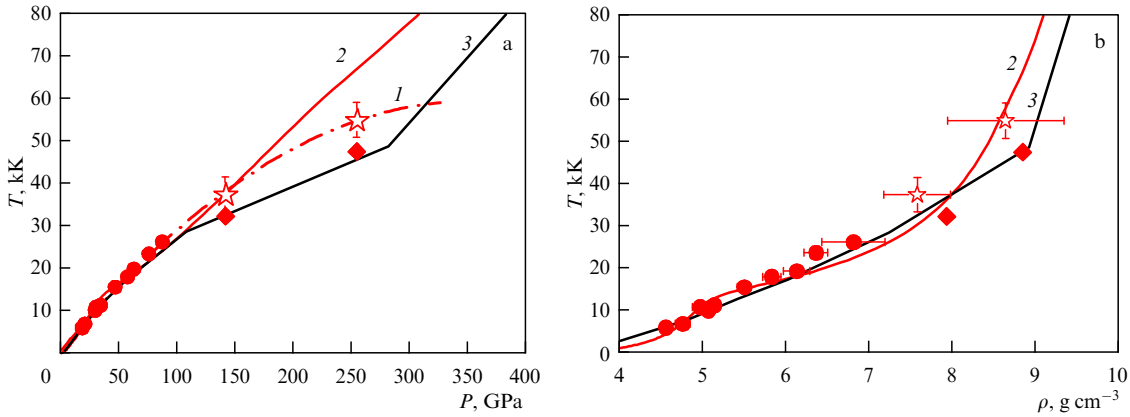

Figure 18. Temperature of shock-compressed liquid krypton as a function of pressure (a) and density (b). Experiment: red dots — flat SWG [45]; red stars — hemispherical SWG [46]. Calculation: *1* — approximation (3.5), *2* — SAHA model [46], red diamonds — QMD [46], *3* — QMD calculation [36].

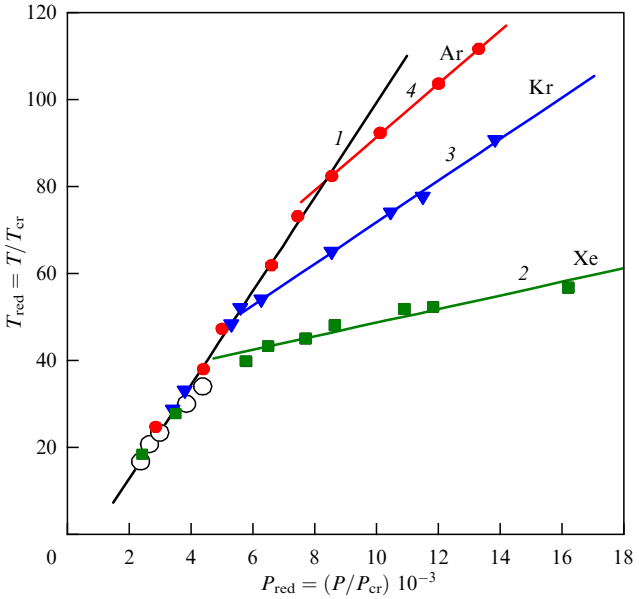

Figure 19. Dependence of temperature of shock-compressed liquefied gases on pressure in reduced coordinates. Experiment: white dots — [26], red dots — [38], blue triangles — [43], green squares — [40, 41]. Approximations: *1* — averaged dependence (4.6), *2* — (4.7), *3* — (4.8), *4* — (4.9).

studies of the temperature of noble gases for the red region of the spectrum in the reduced coordinates $T_{\rm red} = T/T_{\rm cr}$ and $P_{\rm cr} = P/P_{\rm cr}$ are shown in Fig. 19. The values of the critical parameters from [59] were used.

For values of $P_{\rm red} \leqslant 9$, as can be seen from the figure, 16 experimental values for argon [26, 40], krypton [45], and xenon [42, 43] lie on the same straight line (line *1*), which can be represented with a confidence probability of 90% by the regression equation

$$T_{\rm red}(P_{\rm red}) = -(8.999 \pm 1.41) + (10.77 \pm 0.32) P_{\rm red} \times 10^3 . \quad (4.6)$$

Deviation from the law of corresponding states is observed first for xenon, then for krypton and argon. With a confidence probability of 90%, the approximating expressions are as follows:

for liquid xenon (line *2*) at $P_{\rm red} > 3.5$:

$$T_{\rm red}(P_{\rm red}) = (29.37 \pm 1.82) + (2.01 \pm 0.21) P_{\rm red} \times 10^3 , \quad (4.7)$$

for liquid krypton (line *3*) at $P_{\rm red} > 5.6$:

$$T_{\rm red}(P_{\rm red}) = (23.77 \pm 1.50) + (4.78 \pm 0.14) P_{\rm red} \times 10^3 , \quad (4.8)$$

for liquid argon (line *4*) at $P_{\rm red} > 8$:

$$T_{\rm red}(P_{\rm red}) = (28.86 \pm 0.95) + (6.24 \pm 0.09) P_{\rm red} \times 10^3 . \quad (4.9)$$

The intersection of approximations (4.7)–(4.9) with the general approximation (4.6) determines the pressure regions from which deviations from the law of the corresponding states begin: $P_{\rm red} = (8.34 \pm 0.52) \times 10^3$ in argon, $P_{\rm red} = (5.47 \pm 0.27) \times 10^3$ in krypton, $P_{\rm red} = (4.38 \pm 0.18) \times 10^3$ in xenon. These values correspond to pressures $P = (40.0 \pm 2.5)$ GPa for argon, $P = (29.4 \pm 1.5)$ GPa for krypton, $P = (25.0 \pm 1.0)$ GPa for xenon.

Liquid nitrogen. Up to pressures of $P \approx 40$ GPa, radiation from the SW front was recorded in the red region of the spectrum [47], and the data (red dots) shown in Fig. 20 refer to brightness temperatures, which do not take into account the emissive capacity of the shock wave front. In the pressure range of ~ 90 GPa and higher, a five-channel high-speed pyrometer was used in the experiments [59], which made it possible to measure the temperature of shock-compressed liquid nitrogen taking into account the emissive capacity [47]. For experiments with hemispherical SWGs, the refined values of the temperatures T and the emissive capacity $\mathcal{E}$ from [47] are presented in the table and in Fig. 20 together with the known experimental and calculated data.

When processing the data shown in the table, for experiment No. 1, the radiation amplitudes in the section (*1*–*2*) were averaged (see inset a in Fig. 20). When analyzing the results in experiments Nos 1, 2, and 3, the approximation $\mathcal{E} = \text{const}$ was used for the emissive capacity; in experiment No. 4, the model equation $\mathcal{E} = \exp(a_0 \lambda)$, where $a_0 = -2.0 \times 10^{-3}$ nm^{-1} ($[\lambda]$ is measured in nm). In the calculation of this experiment in the wavelength range of 406–600 nm, the average value of the emissive capacity $\mathcal{E}_{\rm sr} = 0.371$ was used.

All experimental data in the pressure range up to 90 GPa are well described by the calculation [48], which used a generalization of the modified van der Waals model to the case of chemically- and ionization-reacting mixtures [93]. In this same region, the experimental results [30, 47–49] are in good agreement with each other and with the calculation [41]. In the region above 90 GPa, calculation [48] predicts higher shock compression temperatures.

Table. Temperature of shock-compressed liquid nitrogen.

No.	Screen	T, K	$\mathcal{E}$	P, GPa
1	Al	16,170 ± 886	0.315 ± 0.037	88.5
2	Fe	24,590 ± 520	0.594 ± 0.036	133
3	Al	30,250 ± 2700	0.205 ± 0.028	160
4	Al	56,560 ± 9585	0.371	265

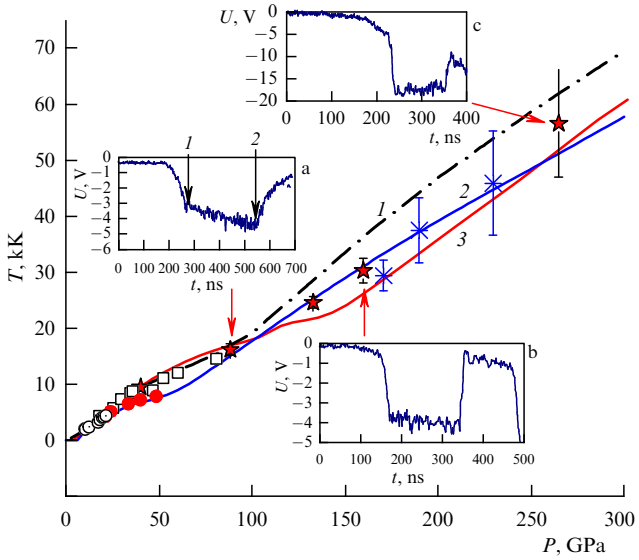

Figure 20. Dependence of temperature of shock-compressed liquid nitrogen on pressure. Experiment: white dots — [26], white squares — [30], red dots — [47], red stars — [47], ✳ — [49]. Calculation: *1* — [30], *2* — [47], *3* — [49].

Earlier in [47] the SAHA-N model was used to describe the parameters of the state of shock-compressed nitrogen and its thermodynamic properties. The thermodynamic description in this model is based on the quasi-chemical representation of nitrogen fluid as a partially ionized thermodynamically equilibrium plasma consisting of atoms, molecules, and atomic and molecular nitrogen ions and electrons, with a strong Coulomb interaction, intense short-range repulsion of heavy particles, and partial degeneracy of electrons. Recent study [49] reports new experimental $T(P)$ data and calculations for shock-compressed gaseous nitrogen with an initial density close to the liquid density, $\rho_0(N_2) = 0.8$ g cm^{-3}. In [49], the N_3 molecule was included in the molecular component — which contains in [47] only diatomic complexes — the repulsion parameters for which (molecule size and repulsion 'softness') were chosen in accordance with its structural data. Figure 20 shows that the experimental data [49] are in good agreement, in the $T-P$ coordinates, with the previous results, and the entire set of results above 90 GPa coincides well with the calculation.

The insets in Fig. 20 show typical oscillograms of the SW front radiation in liquid nitrogen in the pressure range of ≈ 90 GPa and higher. As can be seen from the oscillograms, the behavior of the radiation growth at the shock wave front changes in the experiments. In the experiment at a pressure of $P = 88.5$ GPa (inset a), a sharp increase in radiation over ~ 100 ns is replaced by a slower increase over the next ~ 250 ns. At pressures of 162 and 265 GPa (insets b, c), the growth is followed by a section with a virtually constant radiation level. The difference in the behavior of the oscillograms can be qualitatively explained by the dissociation of nitrogen. In the first case, the sharp increase in radiation (and temperature) is associated with the ionization of the original molecules, while the subsequent increase in the section (*1–2*) is due to the ionization process of the atoms formed during dissociation. As noted earlier in Section 2, the calculation [77] shows that, at a pressure of 90 GPa, half of the molecules are already dissociated, and at pressures of $P \approx 120$ GPa, the dissociation is complete. This implies that the increase in the number of electrons, with which the radiation mechanism is associated, up to the specified pressure is determined by ionization from molecules and atoms, and at higher pressures, from atoms alone. The nature of the radiation of the shock wave front can also alter.

Absorption and reflection of light. Despite the increase in the number of publications on the study of the radiative characteristics of a shock wave front in condensed media, temperature studies still make up only a small part of the total amount of experimental information. Other characteristics of the shock wave front, namely, the absorption and reflection of light in a shock-compressed substance, have been studied experimentally even less.

When determining the true temperature from the measured brightness, the emissive capacity $\mathcal{E}(\lambda, T)$ must be estimated in some way (see Eqn (4.1)), which is often a challenging task under the conditions of an experiment on shock compression. Therefore, the temperature of the shock wave front is usually calculated from the value of $\mathcal{E}$, selected for a better description of the measured spectral temperatures, and, given a weak dependence on wavelength, the value is found:

$$\mathcal{E}(\lambda, T) = \mathcal{E}(T) = \text{const}\,. \tag{4.10}$$

Thus, when describing experimental temperatures, the relationship between the adjustable parameter $\mathcal{E}$ and the value of the absorption coefficient $\mathcal{E}^*$, determined from the main thermodynamic relationship, must be determined:

$$\mathcal{E}^* + \tau + R = 1\,. \tag{4.11}$$

Since the values of emissive capacity $\mathcal{E}$ and absorptivity $\mathcal{E}^*$ are equivalent in the state of thermodynamic equilibrium, $\mathcal{E}$ can be estimated from Eqn (4.11) if the reflectivity R and transparency of the emitting body τ are measured. Previously, the transparency, reflection, and refraction of light of shock-compressed ionic crystals, glass, and some liquids were studied by S.B. Kormer et al. [86].

In studies of the light absorption coefficient in shock-wave experiments, attention is focused on the initial section of the increase in radiation intensity (region 0–*1* in Fig. 1c), which, as in [86], was associated with an increase in the layer of matter compressed by the shock wave and having an (averaged) absorption coefficient α. The radiation intensity of a flat layer in the direction of the normal is described by the formula

$$N = \mathcal{E}N_0 = N_0\,[1 - R - \tau]\,. \tag{4.12}$$

If reflection is ignored and the radiation transmission is determined using the Beer–Lambert–Bouguer formula,

$$\tau = \exp\,(-\alpha l)\,, \tag{4.13}$$

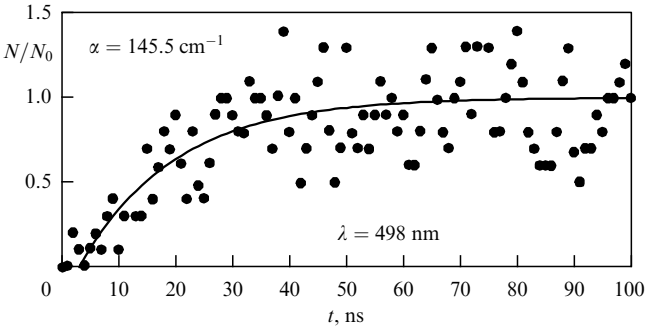

Figure 21. Oscillogram of radiation of shock wave front in liquid argon (for clarity, shown as dots): • — experiment; solid line — approximation.

where α is the coefficient of radiation absorption by a layer of thickness l, Eqn (4.12) can be represented as

$$N = N_0\left[1 - \exp\left(-\alpha l\right)\right] = N_0\left[1 - \exp\left(-\alpha\left(D - U\right)t\right)\right]. \tag{4.14}$$

Here, N_0 is the radiation intensity of the optically dense layer, $l = (D - U)t$ is the thickness of the shock-compressed substance layer, and t is the time of shock wave travel through the substance. From (4.14), it is easy to derive an expression for estimating α:

$$\alpha = -\frac{1}{(D - U)t}\ln\left(1 - \frac{N}{N_0}\right). \tag{4.15}$$

A typical oscillogram of the increase in radiation brightness at the shock wave front, for example, in liquid argon in an experiment with a spherical shock wave generator, and the calculated dependence N/N_0 are displayed in Fig. 21 ($P = 206$ GPa). To calculate the absorption coefficient, the time variation of intensity N/N_0 in (4.15) was determined from oscillograms, and D and U were found from compressibility experiments.

The results of processing the experiments for argon, krypton, and nitrogen are shown in Fig. 22. The measured absorption coefficient of light in liquid krypton, depending on the temperature in the red, blue, and green regions of the spectrum, varied from 10 to 300 cm^{-1} at pressures up to 80 GPa. The approximation dependence is plotted in the same figure:

$$\ln\alpha = (7.0 \pm 0.2) - (2.2 \pm 0.2)\left(\frac{10^4}{T}\right),\ ([\alpha] - \text{cm}^{-1}, [T] - \text{K}). \tag{4.16}$$

At pressures up to ≈ 250 GPa, the coefficient of light absorption in shock-compressed liquid argon varied with temperature from ≈ 3 to 180 cm^{-1}. The approximation dependence of these data is

$$\ln\alpha = (5.71 \pm 0.10) - (1.70 \pm 0.07)\left(\frac{10^4}{T}\right),$$
$$([\alpha] - \text{cm}^{-1}, [T] - \text{K}). \tag{4.17}$$

In liquid nitrogen at pressures up to 100 GPa, the absorption coefficients are lower than in the monatomic cryogenic liquids argon and krypton. However, at the highest studied pressure of 160 GPa, the experimental value of the absorption coefficient of shock-compressed molecular liquid nitrogen lies on the curve of dependence for atomic liquid argon. Qualitatively, this confirms the conclusion about the dissociation process completed in this pressure range [47].

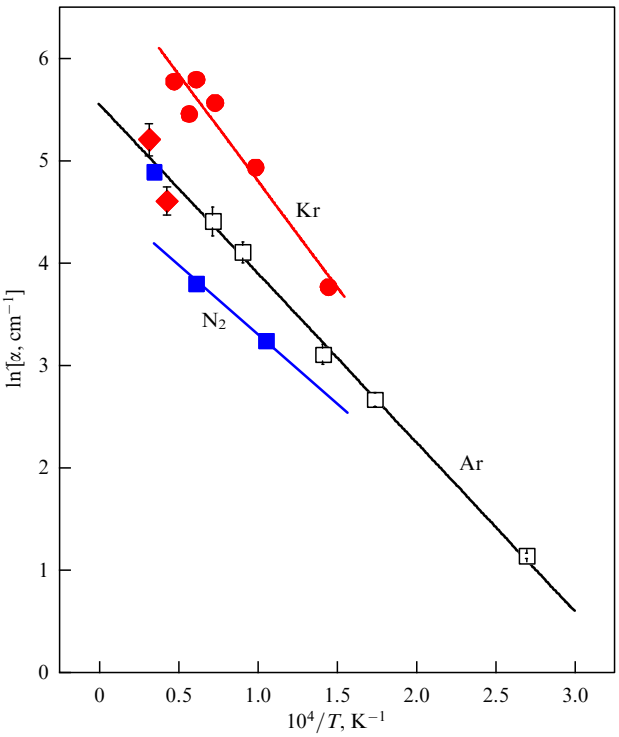

Figure 22. Coefficient of light absorption in shock-compressed liquefied gases. Experiment: red dots — [45], white squares — [40], red diamonds — [41], blue squares — [47]. Solid lines — approximations.

As in the study of ionic crystals [86, 87], a strong temperature dependence of the light absorption coefficients in argon and krypton was observed. Using the technique described above, at a pressure of shock compression of liquid xenon $P = 95$ GPa [44], the coefficient of light absorption in the blue region of the spectrum $\alpha \sim 400$ cm^{-1} was observed.

The reflective properties of the shock wave front in liquid krypton were first studied in [45]. The reflection was measured using the proper luminescence of the SW front (Fig. 23a). The radiation of the SW front (*4*), reflected at an angle of $\sim 10°$ from a copper mirror (*3*) located in the volume of liquid (*2*), was output to an external mirror (*5*) and then to the input lens of a high-speed photo recorder. The radiation of the shock wave front itself was concurrently recorded. It is evident from the figure that the brightness in the k–m section is determined by the radiation of the front and the light reflected from the copper mirror (*3*), while in the m–n section, it is only determined by the luminescence of the front. The intensity of the total radiation in the k–m section can be estimated using the formula

$$N = N_0[1 + \xi R](1 - r), \tag{4.18}$$

where N_0 is the radiation of the shock wave front itself, and ξ, R, and r are the reflection coefficients for the copper mirror, the shock wave front, and the free boundary. The image photometry (Fig. 23b) was carried out across the film.

In the experiment, a jump in the blackening density associated with the reflection of light from the shock wave

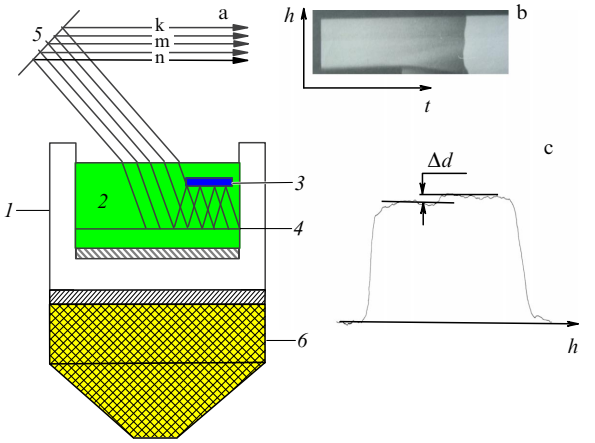

Figure 23. Schematic for measuring light reflection from shock wave front [45]: (a) experimental setup: *1* — cryostat, *2* — liquefied gas, *3* — copper mirror, *4* — shock wave front, *5* — outer mirror, *6* — flat SWG; (b) radiation photochronogram; *h* — direction of film scanning; (c) densitogram (Δd is jump in film blackening density).

front in liquid krypton was clearly recorded (Fig. 23c), and the light reflectivity was measured to be $\sim 13\%$ at a pressure of 76 GPa [45]. In a similar experiment in liquid xenon at a pressure of 67.5 GPa, the light reflectivity from a plane shock wave was measured to be $\sim 20\%$ [45].

5. Electrical conductivity of nitrogen, argon, krypton, and xenon under shock compression in pressure range up to 100 GPa

In shock wave physics, the conventional measurement of the velocity,

$$D = V_0 \left[\frac{P - P_0}{V_0 - V} \right]^{1/2}, \tag{5.1}$$

is essentially a measurement of the derivative, so the value of D is very sensitive to the phase state of the substance. The Hugoniot adiabats of many materials are well described by a linear relationship between D and U, so any deviation from linearity requires attention, since it can imply a change in the aggregate state of the substance. In studying transparent materials, phase transitions can be detected by measuring the temperatures of shock-compressed materials. Both methods were used in the investigation of shock-compressed liquefied gases and showed a fairly significant thermal excitation of electrons in the conduction band. Data on the density of conduction electrons and the behavior of the energy gap depending on the density and temperature, which is important for the theoretical description of experimental results, can be obtained by measuring electrical conductivity. This additional information leads to greater certainty in assessing the role of free electrons. Significant conductivity of liquid argon at a pressure of $P \sim 20$ GPa was already observed in [15]. In [30], a change in conductivity in shock-compressed liquid nitrogen from $G \approx 1.5 \times 10^{-3}\ \Omega^{-1}\ \text{cm}^{-1}$ at $P \approx 20$ GPa to $G \approx 47\ \Omega^{-1}\ \text{cm}^{-1}$ at $P \approx 62$ GPa was observed. The conductivity of liquid oxygen $G \approx 80\ \Omega^{-1}\ \text{cm}^{-1}$ at pressures up to $P \approx 43$ GPa was measured in [31].

In experiments on measuring the electrical conductivity of noble gases and nitrogen conducted at VNIIEF, the technique proposed by L.A. Gatilov and L.V. Kuleshova [94] was used. The elements of the measuring circuit, mounted in a cryostat filled with liquefied gas, and the circuit of the plane-wave experiment are presented in Fig. 24.

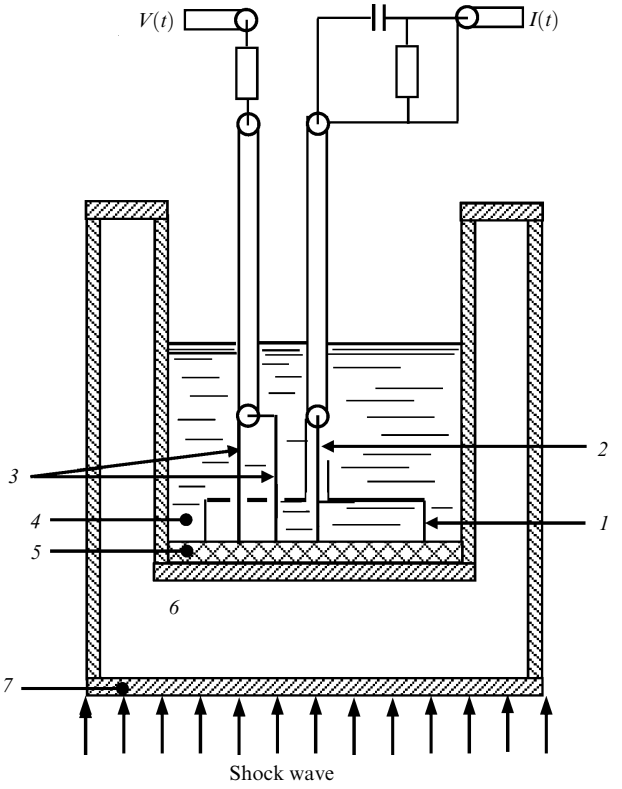

Figure 24. Experimental setup for measuring electrical conductivity of shock-compressed cryogenic liquids: (*1–2*) — current electrodes, *3* — potential electrodes, *4* — liquefied gas, *5* — dielectric, *6* — screen, *7* — striker.

The experimental setup recorded the pulse current $I(t)$ flowing through a sample of shock-compressed liquefied gas (*4*) between a coaxial copper electrode (*1*) and a central electrode (*2*) and the potential difference $V(t)$ between two copper (*3*) probes. The discharge circuit was closed when the shock wave front reached the boundary between the liquid sample (*4*) and the dielectric plate (*5*). The dielectric prevents shunting of the test substance conductivity by the metal screen (*6*), through which the shock wave was output into an experimental cell. The pressure was determined applying the $P-U$ relationships for the test substances, screen materials, and dielectric plate materials using the reflection method. Cooling of the design elements to liquefied gas temperatures was taken into account.

Noble gases. Experimental data from VNIIEF on the electrical conductivity of liquid argon, krypton, and xenon as a function of the shock wave amplitude and temperature are presented in Fig. 25 [50, 51]. It is evident from the figures that the experimental dependences of the electrical conductivity with increasing shock wave pressure tend to saturate at a level of $G \sim 6 \times 10^2\ \Omega^{-1}\ \text{cm}^{-1}$ for xenon at a pressure of $P \sim 40$ GPa, and for krypton, at a pressure of $P \sim 70$ GPa. For argon, this pressure probably exceeds ~ 100 GPa.

In the experimental dependences $G(1/T)$, sections of linear change in electrical conductivity with temperature can be identified, and the electrical conductivity in these sections can be described using a dependence typical of semiconduc-

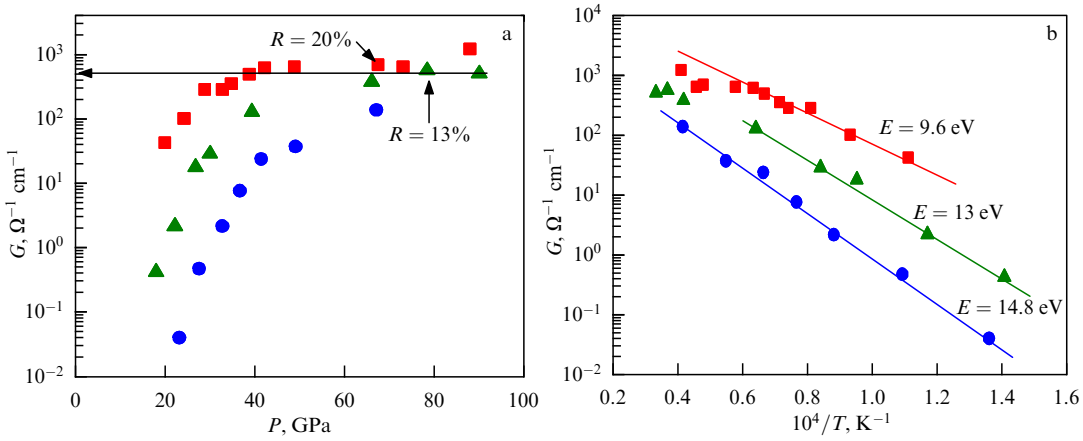

Figure 25. Dependence of electrical conductivity of shock-compressed liquefied noble gases on shock wave amplitude (a) and temperature (b). R — coefficient of light reflection from shock wave front. Experiment [50, 51]: blue dots — Ar, green triangles — Kr, red squares — Xe.

tors:

$$G = G_0 \exp\left(-\frac{E(T,V)}{2kT}\right), \tag{5.2}$$

where $E(T,V)$ is the energy gap between the valence band and the conduction band, and G_0 depends weakly on temperature. The experimental points on the linear sections were approximated using the least squares method with a confidence level of 90%. The approximation dependences were used to determine the width of the energy gaps in each of the gases studied: $E = (14.8 \pm 0.5)$ eV for argon, $E = (13.0 \pm 0.8)$ eV for krypton, and $E = (9.6 \pm 0.5)$ eV for xenon. The data obtained are in satisfactory agreement with the experimental values of the energy gaps measured in observing photoconductivity [95, 96]: $E_0 = 13.4$ eV for argon, 11 eV for krypton, and 9.22 eV for xenon.

Shock-wave compression provides unique opportunities for exploring the transition of dielectrics to the metallic state, since an increase in density is accompanied by a significant increase in temperature and the number of free electrons. This leads to a 'smearing' of the insulator-metal transition forming the prerequisites for observing a continuous transition of dielectrics to the metallic state [97]. An increase in the number of free electrons should lead in this case to an increase in the coefficient of light reflection from the shock wave front, which can be observed experimentally. As shown in Section 2, at pressures up to $P \sim 100$ GPa, the reflection of light from the shock wave front in liquid krypton and xenon is as high as $R \sim 13-20\%$ [45]. Such high light reflection coefficients correspond to pressures at which saturation of electrical conductivity $G(P)$ is observed in krypton and xenon (Fig. 25a). This may be due to the formation of a highly reflective metallic surface at the shock wave front with an increase in the number of free electrons, as in conventional semiconductors with increasing temperature.

Experimental results on the electrical conductivity of shock-compressed noble gases on shock adiabats and along isotherms with various temperatures are displayed in Fig. 26, where these data are compared with the results of other measurements and with calculations using various theoretical models [9]. The figure also shows the boundary of the Coulomb nonideality parameter $\Gamma_D = E_C/E_T = 1$, when the energy of the Coulomb interaction of particles $E_C = e^2/r_D$ ($r_D = (4\pi e^2 \sum Z_i^2 n_i/k_A T)^{-1/2}$ is the Debye radius) is comparable to the average kinetic energy of thermal motion $E_T \sim k_B T$, and the boundary of complete degeneracy of electrons $n_e \lambda_e^3 = 1$, reflecting the change in statistics with increasing pressure; the scale of the kinetic energy of the particles is now the Fermi energy

$$E_F = \frac{\hbar^2 (3\pi^2 n_e)^{2/3}}{2m_e}.$$

The boundaries of the Spitzer electrical conductivity G_{sp}, plotted in Fig. 26, show the influence of density effects on the properties of condensed inert gas plasma. A common feature of the behavior of the experimental data is a sharp increase (by 3 to 5 orders of magnitude) in the specific electrical conductivity of the plasma of liquid argon, krypton, and xenon during compression, which reaches the values of $G \sim 10^2 - 10^3$ Ω^{-1} cm^{-1}, characteristic of alkali metals, in a narrow range of densities: $\rho \sim 2-4$ g cm^{-3} in argon, $\rho \sim 4-8$ g cm^{-3} in krypton, and $\rho \sim 5-10$ g cm^{-3} in xenon. The obtained data exhibit a clearly expressed threshold effect in density and qualitatively contradict the models of weakly nonideal plasma, for which, at low degrees of ionization [99],

$$a_i = \frac{n_e}{(n_e + n_a)} \ll 1, \tag{5.3}$$

the electrical conductivity G is determined by the scattering of electrons on neutral particles and is qualitatively described by the Lorentz formula [3], which predicts a linear dependence of the conductivity on the concentration of free carriers: $G \sim a_i \sim 1/\rho$. As an example, the dependence of the electrical conductivity of an ideal argon plasma is plotted in Fig. 26a (solid red line).

To describe the electrical conductivity of liquefied noble gas plasma under the conditions of the VNIIEF experiments, a quasi-chemical model of nonideal plasma [53, 101–103] was used in [9], taking into account the effects of free electron degeneracy, the Coulomb interaction of charged particles, and the repulsion of heavy particles at short distances, which is due to the overlap of the electron shells of atoms and ions at high densities. To describe the plasma composition, the SAHA ionization equilibrium equation was used [98]:

$$\frac{n_e n_i}{n_a} = \frac{2Q_i}{Q_a} \lambda_e^{-3} \exp\left[-\frac{I - \Delta I(n_e, n_i, T)}{k_B T}\right], \tag{5.4}$$

where Q_i and Q_a are the partition functions of the ion and atom, I is the ionization potential, and ΔI is the decrease in the

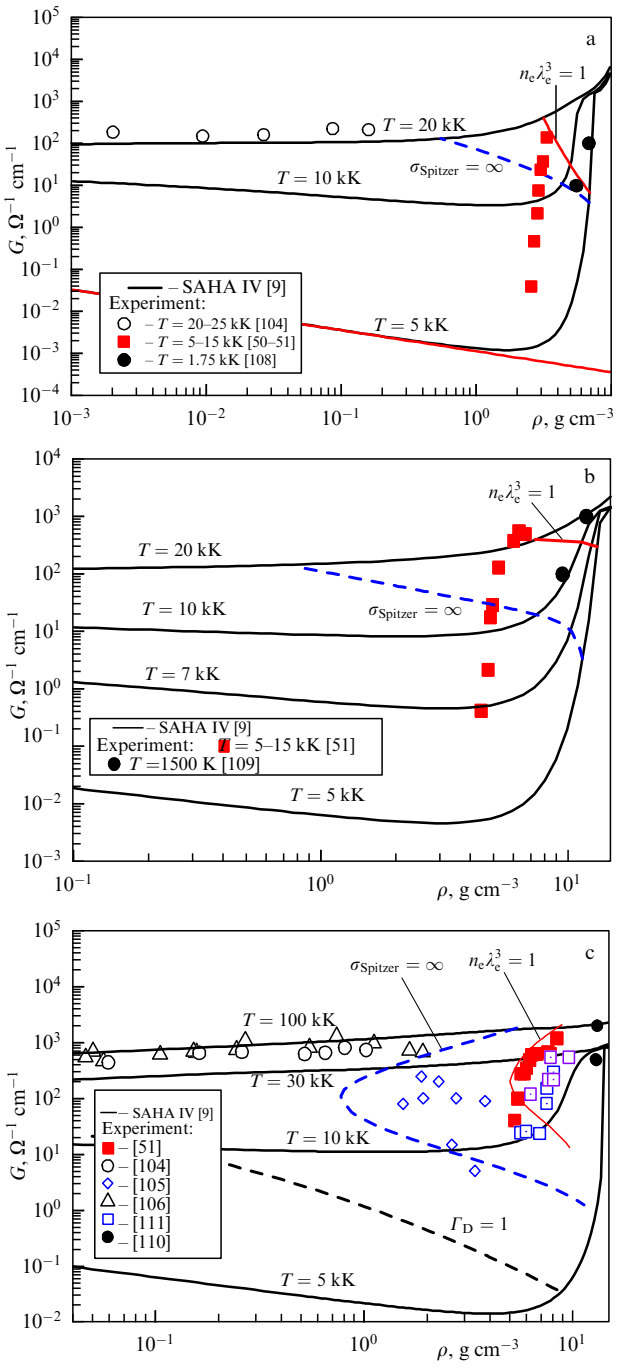

Figure 26. Dependence of specific conductivity of noble gases on density [9]: (a) argon, (b) krypton, (c) xenon.

ionization potential due to interparticle interaction. Taking into account nonideality when determining the plasma composition necessitates the introduction of a density-dependent decrease in the ionization potential ΔI, which leads to an increase in the nonthermal degree of ionization. In this case, a minimum appears on the dependences of electrical conductivity on density at $T = \text{const}$, the depth of which depends on the plasma temperature. As the temperature increases to $T = 20{,}000$ K (see Fig. 26), this minimum is smoothed out when thermal ionization at $k_B T \sim I$ prevails over the effect of pressure ionization, which is significant at $k_B T \ll I$.

As the density increases at a fixed temperature, the ionization processes are completed, and for strong ionization ($a_i \sim 1$) of a weakly nonideal plasma, the Spitzer approximation (nondegenerate plasma) is valid instead of the Lorentz formula [3]:

$$G = \gamma(Z)\,\frac{4\sqrt{2}}{\pi^{3/2}}\,\frac{(k_B T)^{1/2}}{Z m_e e^2}\,\frac{1}{\Lambda}\,,$$

and, in the case of Fermi statistics, the electrical conductivity tends to

$$G \sim \frac{n_e}{\Lambda}\,, \tag{5.5}$$

where Λ is the Coulomb logarithm. This implies that, at high temperatures, the exponential dependence of electrical conductivity described by the Lorentz formula is replaced by a weak logarithmic dependence on the carrier concentration. Under these conditions, the so-called 'minimum metallic' Regel–Ioffe conductivity [99], widely used in the physics of simple metals and semiconductors, can be used as an estimate of conductivity:

$$G \sim \frac{n_e R_s}{v_T}\,, \tag{5.6}$$

where R_s is the radius of the Wigner–Seitz cell, and v_T is the thermal velocity of the electron.

Figure 26 also shows data on the electrical conductivity of singly and doubly compressed plasma of gaseous argon and xenon [103–105], in which temperatures almost an order of magnitude higher than those during compression of condensed gases are realized. In such a case, the effect of thermal ionization comes to the fore, which is most clearly manifested with an increase in the molecular weight of the substance. For example, for xenon (see Fig. 26) at temperatures $T \sim (4-10) \times 10^4$ K, the electrical conductivity reaches values of $G \approx 10^3\ \Omega^{-1}\ \text{cm}^{-1}$ already at densities of $\rho \sim 0.04-1$ g cm^{-3}. For condensed xenon, the same level of electrical conductivity is achieved at $T \sim 10^4$ K and densities $\rho \sim 10$ g cm^{-3}. As can be seen from Fig. 26, with an increase in the molecular weight of the elements, the jump in electrical conductivity during pressure ionization decreases, reaching only two orders of magnitude in xenon. The effect of pressure ionization and the corresponding sharp increase in electrical conductivity are quite noticeable at low temperatures $T < I$, where I is the ionization potential, and at high plasma densities $\rho \sim 1$–10 g cm^{-3}. It should be noted that the plasma ionization model based on the Lorentz formula and the particle composition from Eqn (5.4) leads to an exponential dependence of electrical conductivity on temperature, characteristic of semiconductors [106] during their thermal excitation, with the gap value decreasing with increasing density. The results of this study confirm this conclusion.

Nitrogen. Experimental results on the electrical conductivity of shock-compressed liquid nitrogen in the wake of a plane shock wave [47] depending on the shock wave amplitude are presented in Fig. 27 together with data from [30, 31].

Due to the high mobility of electrons, the electrical conductivity of liquid nitrogen apparently has an electronic nature. In the investigated region of densities up to $\rho \sim$ ~ 2.5 g cm^{-3}, the concentration of nitrogen molecules is $N \sim (3-5) \times 10^{22}$ cm^{-3} and, consequently, the mean free path of electrons l changes insignificantly, remaining relatively constant: $\sim 4 \times 10^6$ cm ($l \sim N^{-1/3}$). Therefore, the observed increase in electrical conductivity by ~ 4 orders of magnitude is completely determined by the increase in the concentration of electrons and depends weakly on the change

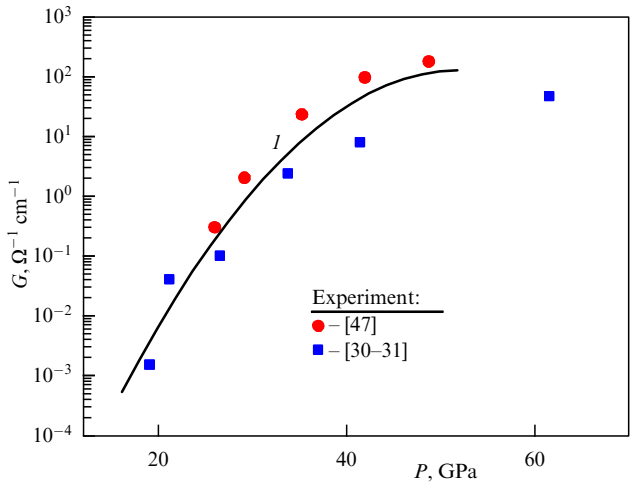

Figure 27. Dependence of electrical conductivity of liquid nitrogen on pressure: *1* — approximation of data from [30] and [47].

in their mobility; with ionization, is related to molecules up to pressures of $P \approx 30$ GPa; and, above that pressure, to both molecules and atoms arising from the dissociation of molecular nitrogen. The absolute values of electrical conductivity measured in [45] at low pressures $P \sim 20$ GPa coincide, and at higher pressures are slightly higher than those in the experiments in [30]. This difference may be due to the features of the measuring circuits used in [30] and [45].

6. Conclusions

This review presents ways to solve the scientific and technical problem related to experimental examination of the states of high energy concentration in plasma under shock compression. The set of experimental data obtained was used to test the parameters of the equations of state of noble gases and nitrogen in a wide range of states up to uniquely high pressures $P \sim 1000$ GPa. To study the shock-wave properties of cryogenic liquids, simple experimental devices of flat and hemispherical geometry have been developed, which have proven convenient for conditions of an experimental testing ground when measuring shock wave velocities on the main and reflected shock adiabats, radiation from the SW front, and electrical conductivity.

In the process of studying the properties of shock-compressed liquid nitrogen, carried out more than 14 years ago [47], first in the pressure range of 100–130 GPa, maximum compression was recorded, after which, with increasing pressure, the $P-\rho$ dependence on the shock adiabat exhibits a virtually isochoric behavior with a compression ratio of $\sigma \approx 4.2$, close to an ideal gas ($\sigma \approx 4$). The combination of experimental and theoretical data [47] suggests that the parameter range $P \sim 100$ GPa, $T \sim 16000$ K, $\rho \sim 3.3$ g cm^{-3} corresponds to the end of the nitrogen depolymerization and its transition to the state of dense nonideal plasma. The data in [47] were later confirmed in VNIIEF experiments with gaseous nitrogen [49]. A distinctive feature of nitrogen as a molecular substance is that it can produce, in addition to the usual molecular crystal and molecular fluid, various forms of the polymer state, which is considered responsible for the existence of shock cooling ('shockcooling') of nitrogen in the reflected shock wave, experimentally observed in [28–30] and recently confirmed in [111]. However, the nature of this transition is not fully understood. At the level of first-principles modeling, the effect of shock cooling was first qualitatively explained in [112]. The study of the transformation of molecular nitrogen at high pressures and temperatures keeps exciting great interest of researchers (see, for example, [113–116]).

The results on the shock compressibility of liquefied noble gases convincingly demonstrate significant thermal excitation of electrons from the valence band to the conduction band in argon at a pressure of $P \approx 40$ GPa and krypton and xenon at pressures of $P \approx (25-30)$ GPa, which can be interpreted as an electronic phase transition leading to an increase in compressibility and a decrease in the rate of temperature increase. Data on the compressibility of liquid argon in a reflected shock wave indicate the need to take them into account when calibrating the EOS under development. This also applies to the development of EOS models and other substances. Studies have shown the high efficiency of high-speed pyrometry for simultaneous experimental measurement of shock wave velocity, sound velocity, temperature, and absorption and reflection coefficients of light in shock-compressed liquefied gases. Measurements of spectral temperatures by a multichannel high-speed pyrometer allowed us to employ in this review the common world practice of finding the temperature by the nonlinear least-squares method for two parameters, T and $\mathcal{E}$, and applying iterations to obtain accurate estimates of the temperature and emissive capacity. A joint analysis of the $D-U$ and $T-P$ dependences shows that the pressure values at which adiabat kinks are observed agree well with each other, and the law of the corresponding states for noble gases is observed at least up to pressures of $P \approx 25$ GPa. The data obtained indicate the relevance of experimental studies of shock compression temperatures in a wide pressure range for testing EOS models.

The reflectivity of the shock wave front was measured up to $R \approx 13-20\%$ in krypton and xenon at shock compression pressures of $P \sim 100$ GPa. The measurements of light absorption and reflection presented above are of independent importance for the development of basic science, and the combination of both quantities makes it possible to estimate the emissive capacity of the shock wave front. This is important when determining their true temperature, which is a more sensitive parameter for testing various theoretical models than just shock pressure. Studies of light reflection and absorption are also of importance for assessing the structure (smoothness) of the shock wave front.

The development of techniques to study electrical conductivity makes it possible to measure the dependence of the energy gap width on density, which, in combination with measuring compressibility and temperature, is necessary to derive a closed equation of state for the substances under study in the megabar pressure region. The experimental data obtained exhibit a sharp increase in the electrical conductivity of nonideal inert gas plasma by 3 to 5 orders of magnitude in a narrow density region due to 'pressure ionization,' which qualitatively disagrees with the models of weakly nonideal plasma. This refers to 'cold' plasma compression ($k_B T \ll I$) in the region of densities and pressures exceeding solid-state ones. In the VNIIEF experiments, an exponential dependence of the electrical conductivity of noble gases on the shock compression temperature was observed, which made it possible to determine the width of their energy gaps in the studied region. These data enable an adequate selection of thermodynamic models for reducing the ionization potential.

The examination of the properties of noble gases and nitrogen at VNIIEF was continued by studying the quasi-

isentropic compressibility of liquid argon and xenon in cylindrical geometry setups. In a series of experiments conducted in the 1990s, liquid argon was compressed to a density of ~ 10 g cm^{-3} under a pressure of ~ 1000 GPa, and liquid xenon to ~ 20 g cm^{-3} under a pressure of ~ 720 GPa [42, 43]. These studies are currently ongoing at VNIIEF. State-of-the-art X-ray technology was used to measure the quasi-isentropic compressibility of krypton in new experiments to a density of ~ 18 g cm^{-3} in a pressure range of up to 2.7 TPa [46]. To achieve terapascal pressures, gaseous krypton in a spherical chamber was compressed by powerful condensed EX. This technique is successfully used at VNIIEF with the participation of the authors in studying the compressibility of helium and deuterium in the pressure range up to 20 TPa (see, for example, [117]). We intend to continue studying the properties of inert gases using a new technique for generating nonideal plasma in the terapascal pressure range and recording the resulting states.

The studies presented above were started at VNIIEF in the mid-1980s on the initiative and under the supervision of Corresponding Member of the USSR Academy of Sciences, Doctor of Physical and Mathematical Sciences, Prof. S.B. Kormer. The development and advancement of experimental methods with the participation of Candidate of Physical and Mathematical Sciences F.V. Grigoriev made it possible to obtain a broad set of experimental data. The data obtained at the initial stage of the research were theoretically interpreted by Doctor of Physical and Mathematical Sciences, Professor V.D. Urlin and his colleague O.L. Mikhailova. Since the 2000s, theoretical support for describing the behavior of inert gases in the megabar pressure range was has been provided by V.K. Gryaznov, V.B. Mintsev, and I.L. Iosilevsky, researchers at the Institute of Problems of Chemical Physics of the Russian Academy of Sciences (Chernogolovka, Moscow region, Russia). Since then, experimental studies have been supported by the Russian Foundation for Basic Research and the Presidium of the Russian Academy of Sciences as part of the comprehensive research program, Physics and Chemistry of Extreme States of Matter, headed at that time by Academician of the Russian Academy of Sciences V.E. Fortov.

A large number of VNIIEF researchers took part in conducting the experiments and processing the obtained data, including V.L. Smirnov, V.D. Glukhodedov, A.B. Kamskov, O.N. Kuznetsov, Yu.A. Grigorieva, A.E. Kovalev, S.I. Kirshanov, T.S. Lebedeva, A.B. Mezhevov, M.G. Novikov, A.N. Shuykin, and V.N. Buzin.

Useful comments on the text of the review were made by Doctor of Physical and Mathematical Sciences V.K. Gryaznov.

The authors express their gratitude and appreciation to all of the above.

References

1. Fortov V E, Yakubov I T *Neideal'naya Plazma* (Non-Ideal Plasma) (Moscow: Energoatomizdat, 1994)
2. Fortov V E *Phys. Usp.* **50** 333 (2007); *Usp. Fiz. Nauk* **177** 347 (2007)
3. Alekseev V A, Fortov V E, Yakubov I T *Sov. Phys. Usp.* **26** 99 (1983); *Usp. Fiz. Nauk* **139** 193 (1983)
4. Fortov V E *Fizika Vysokikh Plotnostei Energii* (High Energy Density Physics) (Moscow: Fizmatlit, 2013)
5. Fortov V E *Extreme States of Matter on Earth and in the Cosmos* (Berlin: Springer-Verlag, 2011)
6. Fortov V E, Iakubov I T *The Physics of Non-Ideal Plasma* (Singapore: World Scientific, 2000)
7. Fortov V *Thermodynamics and Equations of State for Matter*: *From Ideal Gas to Quark-Gluon Plasma* (New York: World Scientific, 2016)
8. Fortov V E et al. *Contrib. Plasma Phys.* **41** 215 (2001)
9. Fortov V E et al. *J. Exp. Theor. Phys.* **97** 259 (2003); *Zh. Eksp. Teor. Fiz.* **124** 288 (2003)
10. Keeler R N *Phys. Usp.* **38** 559 (1995); *Usp. Fiz. Nauk* **165** 595 (1995)
11. Bespalov V E, Gryaznov V K, Fortov V E *Sov. Phys. JETP* **49** 71 (1979); *Zh. Eksp. Teor. Fiz.* **76** 140 (1979)
12. Gryaznov V K et al. *Sov. Phys. JETP* **51** 288 (1980); *Zh. Eksp. Teor. Fiz.* **78** 573 (1980)
13. Dattelbaum D M et al. *AIP Conf. Proc.* **1793** 090004 (2017)
14. Chen Q F et al. *J. Chem. Phys.* **140** 074202 (2014)
15. Keeler R N, Van Thiel M, Alder B J *Physica* **31** 1437 (1965)
16. Van Thiel M, Alder B J *J. Chem. Phys.* **44** 1056 (1966)
17. Nellis W J, Mitchell A C *J. Chem. Phys.* **73** 6137 (1980)
18. Ross M, Nellis W, Mitchell A *Chem. Phys. Lett.* **68** 532 (1979)
19. Ross M *Phys. Rev. A* **8** 1466 (1973)
20. Ross M *J. Chem. Phys.* **73** 4445 (1980)
21. Ross M et al. *J. Chem. Phys.* **85** 1028 (1986)
22. Seitz W, Wackerle W *Bull. Am. Phys. Soc.* **17** 1093 (1972)
23. Dick R D, Warnes R H, Skalyo J (Jr.) *J. Chem. Phys.* **53** 1648 (1970)
24. Nellis W J, van Thiel M, Mitchell A C *Phys. Rev. Lett.* **48** 816 (1982)
25. Zubarev V N, Telegin G S *Sov. Phys. Dokl.* **7** 34 (1962); *Dokl. Akad. Nauk SSSR* **142** 309 (1962)
26. Voskoboinikov I M, Gogulya M F, Dolgoborodov Yu A *Sov. Phys. Dokl.* **24** 375 (1979); *Dokl. Akad. Nauk SSSR* **246** 579 (1979)
27. Dick R D *J. Chem. Phys.* **52** 6021 (1970)
28. Radousky H B et al. *Phys. Rev. Lett.* **57** 2419 (1986)
29. Radousky H B, Ross M *High Pressure Res.* **1** 39 (1988)
30. Nellis W J et al. *J. Chem. Phys.* **94** 2244 (1991)
31. Hamilton D C et al. *J. Chem. Phys.* **88** 5042 (1988)
32. Nellis W J et al. *J. Chem. Phys.* **95** 5268 (1991)
33. Root S et al. *Phys. Rev. B* **106** 174114 (2022)
34. Root S et al. *Rev. Lett.* **105** 085501 (2010)
35. Root S et al., in *Proc. of the Intern. Conf. on Shock Waves in Condensed Matter, Novgorod, 2010*
36. Mattsson T R et al. *Phys. Rev. B* **90** 184105 (2014)
37. Kim Y-J et al. *Phys. Rev. Lett.* **129** 015701 (2022)
38. Yakub E S *Low Temp. Phys.* **19** 377 (1993); *Fiz. Nizk. Temp.* **19** 531 (1993)
39. Boates B, Bonev S A *Phys. Rev. Lett.* **102** 015701 (2009)
40. Grigor'ev F V et al. *Sov. Phys. JETP* **61** 751 (1985); *Zh. Eksp. Teor. Fiz.* **88** 1271 (1985)
41. Gryaznov V K et al., in *Joint 20th AIRAPT – 43rd EHPRG Intern. Conf. on High Pressure Science and Technology, Karlsruhe, Germany, June 27 – July 1, 2005, Abstracts*, p. 55
42. Urlin V D, Mochalov A, Mikhailova L *Matem. Modelirovanie* **3** (7) 42 (1991)
43. Urlin V D, Mochalov M A, Mikhailova O L *High Pressure Res.* **8** 595 (1992)
44. Zhernokletov M V et al, in *Shock Compression of Condensed Matter – 2003, Proc. of the Conf. of the American Physical Society Topical Group on Shock Compression of Condensed Matter* (AIP Conf. Proc., Vol. 706, Eds M D Furnish, M D Gupta, J W Forbes) (New York: AIP, 2004) p. 129
45. Mochalov M A et al., in *Shock Compression of Condensed Matter – 1999* (AIP Conf. Proc., Vol. 505, Eds M D Furnish, C Chhabildas, R S Hixson) (New York: AIP, 2000) p. 983
46. Mochalov M A et al. *JETP Lett.* **119** 885 (2024); *Pis'ma Zh. Eksp. Teor. Fiz.* **119** 854 (2024)
47. Mochalov M A et al. *J. Exp. Theor. Phys.* **110** 67 (2010); *Zh. Eksp. Teor. Fiz.* **137** 77 (2010)
48. Trunin R F et al. *JETP Lett.* **88** 189 (2008); *Pis'ma Zh. Exp. Teor. Fiz.* **88** 220 (2008)
49. Zhernokletov M V et al. *J. Exp. Theor. Phys.* **136** 241 (2023); *Zh. Eksp. Teor. Fiz.* **163** 274 (2023)
50. Gatilov L A et al. *J. Appl. Mech. Tech. Phys.* **26** (1) 88 (1985); *Prikl. Mekh. Tekh. Fiz.* (1) 99 (1985)
51. Mochalov M A et al., in *American Physical Society, Conf. on Shock Compression of Condensed Matter June 28 – July 2, 1999, Snowbird, Utah, Abstracts*, S1.05
52. Kormer S B et al. *Sov. Phys. JETP* **15** 477 (1962); *Zh. Eksp. Teor. Fiz.* **42** 686 (1962)

53. Kormer S B et al. *Sov. Phys. JETP* **21** 689 (1965); *Zh. Eksp. Teor. Fiz.* **48** 1033 (1965)
54. Urlin V D *Sov. Phys. JETP* **22** 341 (1966); *Zh. Eksp. Teor. Fiz.* **49** 485 (1965)
55. Gryaznov V K, Iosilevskii I L, Fortov V E, in *Entsiklopediya Nizkotemperaturnoi Plazmy* (Encyclopedia of Low Temperature Plasma) Vol. III-1 Applications (Ed.-in-Chief V E Fortov, Eds A N Starostin, I L Iosilevskii) (Moscow: Fizmatlit, 2004)
56. Lyon S P, Johnson J D, Group T-1 (Eds) "SESAME: The Los Alamos National Laboratory Equation of State Database," Report LA-UR-92-3407 (Los Alamos, NM: Los Alamos National Laboratory, 1995)
57. Trunin R F (Ed.) *Svoistva Kondensirovannykh Veshchestv pri Vysokikh Davleniyakh i Temperaturakh* (Properties of Condensed Matter at High Pressures and Temperatures) (Arzamas-16: VNII Eksperimental'noi Fiziki, 1992)
58. Al'tshuler L V et al. *Phys. Usp.* **39** 539 (1996); *Usp. Fiz. Nauk* **166** 575 (1996)
59. Zhernokletov M V et al., in *Shock Compression of Condensed Matter — 2001. Proc. of the Conf. of the American Physical Society, Topical Group on Shock Compression of Condensed Matter, Atlanta, Georgia, 24–29 June 2001* (AIP Conf. Proc., Vol. 620, Eds M D Furnish, Y Horie, N N Thadhani) (New York: AIP, 2002) pp. 763–766
60. Gavrilov N F et al. *Vopr. Atom. Nauki Tekh. Ser. Metod. Program. Chisl. Resheniya Zadach Matem. Fiz.* (3) 11 (1982)
61. Vasserman A A, Rabinovich V A *Thermophysical Properties of Liquid Air and Its Components* (Jerusalem: Israel Program for Scientific Translation, 1970); Translated from Russian: *Teplofizicheskie Svoistva Zhidkogo Vozdukha i Ego Komponent* (Moscow: Izd. Standartov, 1968)
62. Rabinovich V A et al. *Thermophysical Properties of Neon, Argon, Krypton, and Xenon* (Berlin: Springer-Verlag, 1988); Translated from Russian: *Teplofizicheskie Svoistva Neona, Argona, Kriptona i Ksenona* (Moscow: Izd. Standartov, 1976)
63. Gordeev D G et al. *Combustion Explosion Shock Waves* **44** 177 (2008); *Fiz. Goreniya Vzryva* **44** (2) 61 (2008)
64. Trunin R F (Ed.) *Eksperimental'nye Dannye po Udarno-Volnovomu Szhatiyu i Adiabaticheskomu Rasshireniyu Kondensirovannykh Veshchestv* (Experimental Data on Shock-Wave Compression and Adiabatic Expansion of Condensed Matter) (Sarov: RFYaTs — VNIIEF, 2001)
65. Knudson M D, Asay J R, Deeney C *J. Appl. Phys.* **97** 073514 (2005)
66. Nellis W J, Mitchell A C, Young D A *J. Appl. Phys.* **93** 304 (2003)
67. Glushak B L, Gudarenko L F, Styazhkin Yu M *Vopr. Atom. Nauki Tekh. Ser. Matem. Model. Fiz. Protsessov* (2) 57 (1991)
68. Jephcoat A P et al. *Phys. Rev. Lett.* **59** 2670 (1987)
69. Zisman A N, Aleksandrov I V, Stishov S M *Phys. Rev. B* **32** 484 (1985)
70. Reichlin R et al. *Phys. Rev. Lett.* **62** 669 (1989)
71. Syassen K *Phys. Rev. B* **25** 6548 (1982)
72. Asaumi K *Phys. Rev. B* **29** 7026 (1984)
73. Goettel K A et al. *Phys. Rev. Lett.* **62** 665 (1989)
74. Blikov A O et al., Patent RU 2545289 C1; *Byull. Izobret.* (9) (2015)
75. Grishechkin S K et al. *JETP Lett.* **80** 398 (2004); *Pis'ma Zh. Eksp. Teor. Fiz.* **80** 452 (2004)
76. Mochalov M A et al. *J. Exp. Theor. Phys.* **125** 948 (2017); *Zh. Eksp. Teor. Fiz.* **152** 1113 (2017)
77. Calef D F, Ree F H *Phys. Rev. B* **36** 4935 (1987)
78. Al'tshuler L V *Sov. Phys. Usp.* **8** 52 (1965); *Usp. Fiz. Nauk* **85** 197 (1965)
79. Zel'dovich Ya B, Raizer Yu P *Physics of Shock Waves and High-Temperature Hydrodynamic Phenomena* (New York: Academic Press, 1966, 1967); Translated from Russian: *Fizika Udarnykh Voln i Vysokotemperaturnykh Gidrodinamicheskikh Yavlenii* (Moscow: Nauka, 1966)
80. Kormer S B et al. *Sov. Phys. JETP* **22** 97 (1966); *Zh. Eksp. Teor. Fiz.* **49** 135 (1965)
81. Nadykto B A, in *Shock Compression of Condensed Matter — 2011. Proc. of the Conf. of the American Physical Society Topical Group on Shock Compression of Condensed Matter, Chicago, Illinois, USA, 2011* (AIP Conf. Proc., Vol. 1426, Eds M L Elert et al.) (Melville, NY: AIP, 2012)
82. McQueen R G et al., in *High-Velocity Impact Phenomena* (Ed. R Kinslow) (New York: Academic Press, 1970) p. 293, https://doi.org/10.1016/B978-0-12-408950-1.50012-4; Translated into Russian: *Vysokoskorostnye Udarnye Yavleniya* (Moscow: Mir, 1973)
83. Model' I Sh *Sov. Phys. JETP* **5** 589 (1957); *Zh. Eksp. Teor. Fiz.* **32** 714 (1957)
84. Roth J *J. Appl. Phys.* **35** 1429 (1964)
85. Tsikulin M A, Popov E G *Izluchatel'nye Svoistva Udarnykh Voln v Gazakh* (Radiative Properties of Shock Waves in Gases) (Moscow: Nauka, 1977)
86. Kormer S B *Sov. Phys. Usp.* **11** 229 (1968); *Usp. Fiz. Nauk* **94** 641 (1968)
87. Kormer S B, Sinitsin M V, Kuryapin A I *Sov. Phys. JETP* **28** 852 (1969); *Zh. Eksp. Teor. Fiz.* **55** 1626 (1968)
88. Zeldovich Ya B, Kormer S B, Urlin V D *Sov. Phys. JETP* **28** 855 (1969); *Zh. Eksp. Teor. Fiz.* **55** 1631 (1968)
89. Kirillov G A, Kormer S B, Sinitsin M V *JETP Lett.* **7** 290 (1968); *Pis'ma Zh. Eksp. Teor. Fiz.* **7** 368 (1968)
90. Radousky H B, Mitchell A C *Rev. Sci. Instrum.* **60** 3707 (1989)
91. Radousky H B, Ross M *Phys. Lett. A* **129** 43 (1988)
92. Voitenko A E, Kuznetsov F O, Model I Sh *Instrum. Exp. Tech.* (6) 1184 (1962); *Prib. Tekh. Eksp.* (6) 121 (1962)
93. Medvedev A B *Vopr. Atom. Nauki Tekh. Ser. Teor. Prikl. Fiz.* (1) 12 (1992)
94. Gatilov L A, Kuleshova L V *J. Appl. Mech. Tech. Phys.* **22** 114 (1981); *Prikl. Mekh. Tekh. Fiz.* (1) 136 (1981)
95. Huang S S-S, Freeman G R *Can. J. Chem.* **55** 1838 (1977)
96. Asaf U, Steinberger I T *Phys. Rev. B* **10** 4464 (1974)
97. Zel'dovich Ya B, Landau L D *Zh. Eksp. Teor. Fiz.* **14** 32 (1944)
98. Fortov V E (Ed.-in-Chief) *Entsiklopediya Nizkotemperaturnoi Plazmy* (Encyclopedia of Low Temperature Plasma) (Moscow: Nauka, 2000)
99. Mott N F, Davis E A *Electronic Processes in Non-Crystalline Materials* (Oxford: Clarendon Press, 1971)
100. Gryaznov V K et al. *Teplofizicheskie Svoistva Rabochikh Sred Gazofaznogo Yadernogo Reaktora* (Thermophysical Properties of Working Media of a Gas-Phase Nuclear Reactor) (Ed. V M Ievlev) (Moscow: Atomizdat, 1980)
101. Gryaznov V K, Iosilevskii I L, Fortov V E, in *Udarnye Volny i Ekstremal'nye Sosotyaniya Veshchestva* (Shock Waves and Extreme States of Matter) (Eds V E Fortov, L V Al'tshuler, R F Trunin, A I Funtikov) (Moscow: Nauka, 2000) p. 342
102. Iosilevskii I L, in *Entsiklopediya Nizkotemperaturnoi Plazmy* (Encyclopedia of Low Temperature Plasma) Introductory Vol. 1 (Ed. V E Fortov) (Moscow: Nauka, 2000)
103. Ivanov Yu V et al. *Sov. Phys. JETP* **44** 112 (1976); *Zh. Eksp. Teor. Fiz.* **71** 216 (1976)
104. Mintsev V B, Fortov V E *JETP Lett.* **30** 375 (1979); *Pis'ma Zh. Eksp. Teor. Fiz.* **30** 401 (1979)
105. Mintsev V B, Fortov V E, Gryaznov V K *Sov. Phys. JETP* **52** 59 (1980); *Zh. Eksp. Teor. Fiz.* **79** 116 (1980)
106. Zeeger K *Semiconductor Physics* (New York: Springer-Verlag, 1973); Translated into Russian: *Fizika Poluprovodnikov* (Moscow: Mir, 1977)
107. Dolotenko M I et al., in *Trudy Sed'moi Mezhdunarodnoi Konf. po Generatsii Megagaussnykh Magnitnykh Polei i Rodstvennym Eksperimentam, Sarov, 5–10 Avgusta 1996 g.* (Proc. of the 7th Intern. Conf. on Megagauss Magnetic Field Generation and Related Experiments, Sarov, August 5–10, 1996) Vol. 2 (Eds V K Chernyshev, V D Selemir, L N Plyashkevich) (Sarov: VNIIEF, 1997)
108. Veeser L I et al., in *Proc. VIII Intern. Conf. on Megagauss Magnetic Field Generation and Related Topics, Tallahasse, 1998*
109. Eremets M I et al. *Phys. Rev. Lett.* **85** 2797 (2000)
110. Mintsev V B et al., in *Shock Compression of Condensed Matter — 1999* (AIP Conf. Proc., Vol. 505, Eds S C Schmidt, D P Dandekar, J W Forbes) (Woodbury, NY: AIP, 2000) p. 987
111. Zhuo-Ning F et al. *Phys. Lett. A* **519** 129700 (2024)
112. Fedorov I D, Stegailov V V *J. Chem. Phys.* **161** 154503 (2024)
113. Jiang S et al. *Nat. Commun.* **9** 2624 (2018)
114. Driver K P, Militzer B *Phys. Rev. B* **93** 064101 (2016)
115. Bergermann A, Redmer R *Phys. Rev. B* **108** 085101 (2023)
116. Melicherová D, Martoňák R *J. Chem. Phys.* **158** 244503 (2023)
117. Mochalov M A et al. *JETP Lett.* **118** 568 (2023); *Pis'ma Zh. Eksp. Teor. Fiz.* **118** 578 (2023)